JGR Solid Earth

RESEARCH ARTICLE
10.1029/2025JB032007

Testing Volcano Deformation Models Against 3D Seismic Reflection Imagery of Ancient Intrusions

C. Magee[1], S. K. Ebmeier[1], and J. Hickey[2]

[1]School of Earth and Environment, University of Leeds, Leeds, UK, [2]Department of Earth and Environmental Sciences, University of Exeter, Exeter, UK

Key Points:

- Seismic reflection data can image ancient intrusions, forced folds, and surface deformation in 3D
- We use volcano deformation models to estimate sources from surface uplift above a seismically imaged laccolith
- We compare modeled and observed sources, showing models simulate reasonably well the source lateral position but not its depth

Supporting Information:

Supporting Information may be found in the online version of this article.

Correspondence to:

C. Magee,
c.magee@leeds.ac.uk

Citation:

Magee, C., Ebmeier, S. K., & Hickey, J. (2026). Testing volcano deformation models against 3D seismic reflection imagery of ancient intrusions. *Journal of Geophysical Research: Solid Earth*, *131*, e2025JB032007. https://doi.org/10.1029/2025JB032007

Received 15 MAY 2025
Accepted 22 JAN 2026

Author Contributions:

Conceptualization: C. Magee, S. K. Ebmeier
Data curation: C. Magee
Formal analysis: C. Magee
Funding acquisition: C. Magee
Methodology: C. Magee, S. K. Ebmeier, J. Hickey
Writing – original draft: C. Magee
Writing – review & editing: C. Magee, S. K. Ebmeier, J. Hickey

Abstract Magma intrusion often drives uplift of the overburden and free surface. Analytical modeling of such surface uplift at active volcanoes allows us to estimate intrusion geometries and positions, as well as volume and pressure changes; these insights have proven critical to forecasting volcanic unrest and eruptions. However, it is rarely possible to compare geodetic source parameters retrieved from analytical models to known intrusion geometries. Seismic reflection data offer an opportunity to image and quantify ancient, buried intrusion geometries and their overburden deformation (i.e., a forced fold). Here, we use 3D seismic reflection data offshore NW Australia to investigate an Early Cretaceous forced fold developed above a laccolith emplaced at ~0.6–1 km depth. We remove the effects of post-emplacement, burial-related compaction and estimate surface displacement patterns for the forced fold. Analytical modeling of these surface displacements, using both thin plate bending and elastic half-space solutions, suggest source (intrusion) estimates of position and lateral dimensions are similar to those of the actual laccolith. There are some differences between measurements of the laccolith and modeled source estimates, which we attribute to syn-intrusion space-making mechanisms (e.g., compaction). We particularly find penny shaped crack and rectangular dislocation elastic half-space solutions underestimate source emplacement depth by ~0.2–0.9 km, probably reflecting a lack of heterogeneity (layering) in our models. Our novel approach highlights seismic reflection data is a powerful tool for understanding and testing how magma emplacement translates into surface deformation at active volcanoes.

Plain Language Summary As magma moves through the crust it pushes up overlying rock, causing the ground to move. We measure these tiny ground movements at active volcanoes and use computer models to predict how they relate to underlying magma body size and location; this provides us important information on whether an eruption may occur. However, the models we use are very simplistic and their results are very difficult to test. Here, we use 3D seismic reflection data, which provides ultrasound-like images of Earth's shallow subsurface, to study a buried, ancient magma body and the overlying rock it pushed upwards. We measure the amount of ground movement generated by the injecting magma. With the same computer models, we use these ground movement measurements to predict underlying magma body size and location. Critically, our 3D seismic data allows us to compare these predicted magma body properties to the actual magma body. Our results show that the position and lateral dimensions of the predicted magma bodies are reasonable to that of the observed magma body. However, the predicted magma body depths are underestimated. Where we use these bodies at active volcanoes, we should thus be aware that the magma may actually be deeper than predicted.

1. Introduction

Space for emplacement of a new magma body, or recharge of an existing reservoir, can be generated by uplift of the overlying rock and free surface (e.g., Hansen & Cartwright, 2006; Karlstrom et al., 2018; Magee et al., 2017a; Mogi, 1958; Pollard & Johnson, 1973; Segall, 2010). The shape and magnitude of such surface displacement relates to the geometry, location, and conditions of the underlying magma intrusion and its host rock properties (e.g., Pollard & Johnson, 1973; Stearns, 1978; Segall, 2010; Galland & Scheibert, 2013; O'Hara et al., 2021). Surface displacements at active volcanoes typically have magnitudes of mm–m and occur over days-to-years (e.g., Biggs & Wright, 2020; Segall, 2013). By modeling measured surface displacement patterns at active volcanoes, we can estimate the subsurface source (intrusion) geometry, depth, volume change, and/or pressure change (e.g., Figure 1a) (e.g., Biggs & Wright, 2020; Lisowski, 2007; Masterlark et al., 2010; Nikkhoo et al., 2016; Segall, 2010; Sparks et al., 2012). These modeled constraints on active volcanic domains are crucial

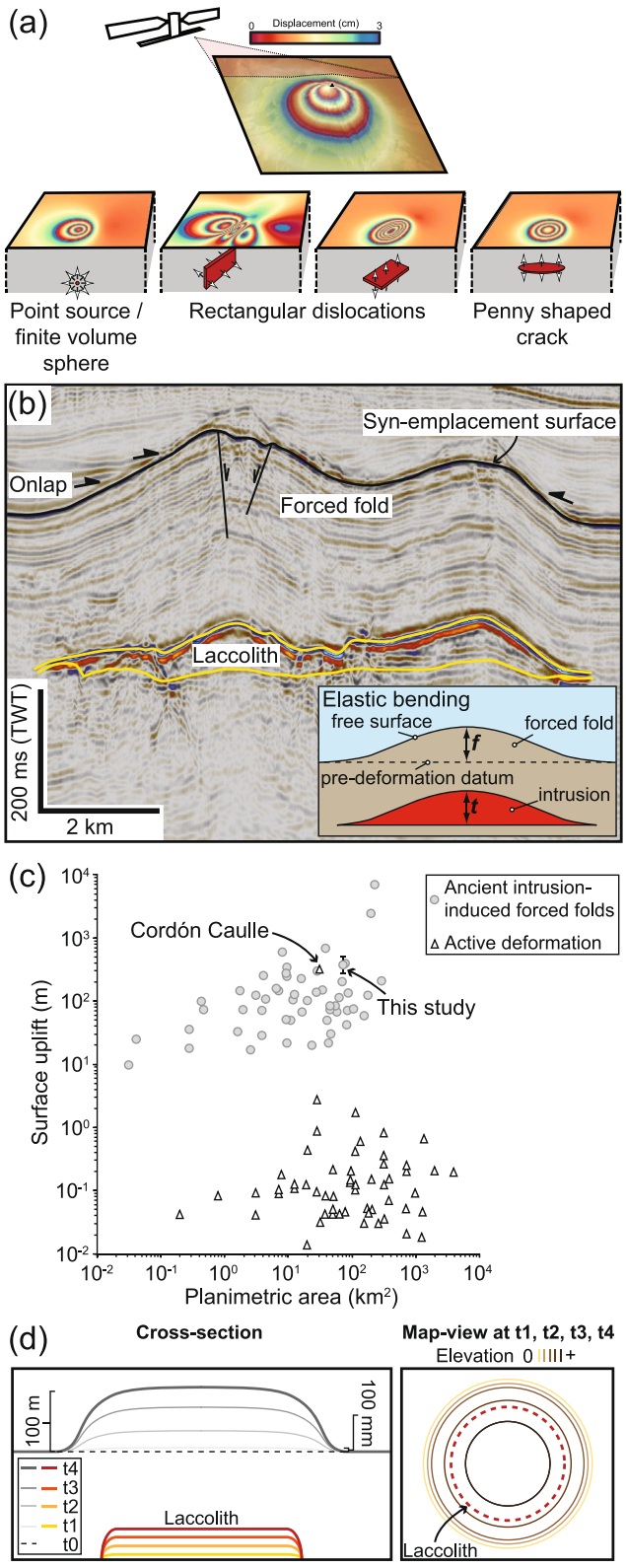

Figure 1.

for forecasting trajectories of unrest and eruption (e.g., Crozier et al., 2023; Ebmeier et al., 2018; Garthwaite et al., 2019; Sparks, 2003).

Many volcano deformation models use analytical approaches that embed simple source geometries within homogeneous, isotropic, and linearly elastic host materials (Figure 1a) (e.g., Crozier et al., 2023; Fialko et al., 2001; Galland & Scheibert, 2013; Masterlark, 2007; Mctigue, 1987; Mogi, 1958; Nikkhoo et al., 2016; Okada, 1985). Of these models, most adopt an elastic half-space framework with a uniform pressure or volume change boundary condition applied to the source, which induces displacement around the entirety of the source (i.e., roof, floor, and side-wall deformation; e.g., Figure 1a) (e.g., Fialko et al., 2001; Hautmann et al., 2010; Hickey et al., 2013; Masterlark, 2007; Mctigue, 1987; Mogi, 1958; Okada, 1985). However, elastic half-space solutions may not be suitable for modeling shallow ($\lesssim$5 km) intrusions, where roof uplift via elastic bending dominates and little or no floor subsidence occurs (e.g., Jackson et al., 2013; Magee et al., 2019; van Wyk de Vries et al., 2014). For such shallow-level, tabular intrusions, some analytical methods apply thin elastic plate bending solutions to simulate displacement (Figure 1b) (e.g., Bunger & Cruden, 2011; Castro et al., 2016; Galland & Scheibert, 2013; Kerr & Pollard, 1998; O'Hara et al., 2021; Pollard & Johnson, 1973; Scheibert et al., 2017; White et al., 2023).

Regardless of whether simple analytical models use an elastic half-space or thin plate bending, we know they are wrong to some extent because: (a) assumptions of homogeneity and isotropy in the crust are rarely valid (e.g., Galland, 2012; Hickey et al., 2016; Manconi et al., 2007; Segall, 2010); and (b) they do not account for synchronous inelastic space-making processes (e.g., compaction, fluidization) (e.g., Currenti et al., 2010; Einsele et al., 1980; Morgan et al., 2008; Schofield et al., 2012). Yet simple analytical models remain widely used because uncertainties in their assumptions (and outputs) are outweighed by their low computational cost, which enable a first-order assessment of source properties in a timeframe pertinent to real-time decision-making during unrest (e.g., Garthwaite et al., 2019; Parks et al., 2023; Taylor et al., 2021). Furthermore, where little is known about the physical properties of the intrusion or surrounding crust, the simplifying assumptions of an elastic half space or thin plate bending model may be preferable to poorly constrained complexity. Whilst simple analytical models

Figure 1. (a) Schematic showing how satellite-based Interferometric Synthetic Aperture Radar (InSAR) data can be used to monitor ground movements at volcanoes, and the expected surface displacement patterns predicted by different source geometries embedded in a homogeneous and isotropic elastic half-space (modified from Magee et al., 2018). (b) Time-migrated seismic reflection image from the Bight Basin, offshore S Australia, showing a buried laccolith and forced fold pair (modified from Jackson et al., 2013). Onlap of overlying reflections onto the forced fold denote its top, that is, the syn-emplacement free surface. Vertical axis is in milliseconds two-way time (ms TWT). Inset: schematic showing fold amplitude (f) (i.e., uplift from the pre-deformation datum) and intrusion thickness (t) are expected to be similar if space for magma was solely generated by elastic bending (Galland & Scheibert, 2013; Pollard & Johnson, 1973). (c) Plot of intrusion-induced surface uplift measured from ancient forced folds, both observed in the field and seismic reflection data, and recorded by InSAR data at active volcanoes (see Table S1 in Supporting Information S1 for data and references). (d) Sketch showing how laccolith and forced fold growth may relate through time. The time gaps between t0, t1, etc… could be hours to millions of years.

do commonly fit observed displacement data, we expect there to be limits to their applicability (e.g., Battaglia & Hill, 2009; Crozier et al., 2023). Independent geophysical data (e.g., gravity), or testing sensitivity using synthetic data or analog models (e.g., Crozier et al., 2023; Poppe et al., 2024), can provide insight into the suitability of an elastic half space or flexure-based approach. However, natural examples where known and modeled source properties can be confidently compared are very rare.

Seismic reflection data allow us to measure ancient, intrusion-induced surface uplift (forced folds) and determine the 3D geometry and location of underlying, solidified magma bodies at meter- to decameter-scale resolutions (Figure 1b) (e.g., Hansen & Cartwright, 2006; Jackson et al., 2013; Magee et al., 2013; Reynolds et al., 2017). Here, we examine an Early Cretaceous laccolith that was emplaced at <2 km depth and uplifted (bended) overlying strata by 100's m across an area of ∼14 km^2 in the Exmouth Plateau sedimentary basin, offshore NW Australia (Dobb et al., 2022). We remove the effect of burial-related compaction to recover the final, pre-burial surface displacement developed over the lifetime of the laccolith (e.g., Magee et al., 2019; Smallwood, 2009). From these decompacted data we calculate syn-emplacement surface elevation changes and use these to extract plausible horizontal components of displacement, which we scale to mm–m based on the assumption of a uniform deformation rate. We aim to test whether our inferred surface displacements are well described by analytical volcano deformation models. Given the laccolithic geometry and shallow emplacement depth of the intrusion, we test the applicability of a thin plate bending solution (Galland & Scheibert, 2013) and penny shaped crack and rectangular dislocation elastic half-space models (e.g., Figure 1a) (e.g., Fialko et al., 2001; Okada, 1985). We show that both analytical approaches, using either thin plate bending or elastic half-space methods, seem to reliably capture intrusion positions and lateral extents, but not emplacement depths. By analytically modeling surface displacement patterns extracted from seismic reflection data, we can compare estimated source properties to the observed parameters of natural intrusions in 3D.

2. Comparing Geodetic and Seismic Reflection Data

2.1. Seismic Reflection Data, Intrusions, and Forced Folds

Seismic reflection data can image igneous intrusions, typically in sedimentary basins, and show that some are overlain by uplifted strata with current reliefs of 10's–100's m (Figures 1b and 1c) (e.g., Hansen & Cartwright, 2006; Jackson et al., 2013; Magee et al., 2019). We term these areas of overburden uplift "forced folds" because their "shape and trend are dominated by the shape of some forcing member (that is, a magma intrusion) below" (Stearns, 1978); by this definition, intrusion-induced uplift and subsidence at active volcanoes can also be categorized as forced folding (e.g., Karlstrom et al., 2018; van Wyk de Vries et al., 2014). Where such forced folds are imaged in seismic reflection data, or exposed at Earth's surface, they typically reveal the total lifetime impact of shallow-level (<4 km depths) intrusions on host rock deformation (Figure 1b). Specifically, these examples show space is primarily generated by overburden uplift, often involving elastic bending (folding) and occasional faulting, with minimal or no floor subsidence (Figure 1b) (e.g., Hansen & Cartwright, 2006; Magee et al., 2013; Magee et al., 2017a; Magee et al., 2018). Critically, the tops of intrusion-induced forced folds are often marked by onlap of overlying reflections, which indicates they represent the syn-emplacement free surface (Figure 1b) (e.g., Hansen & Cartwright, 2006; Jackson et al., 2013; Trude et al., 2003). By removing the effects of burial-related compaction we can thus recover and quantify the final, pre-burial geometry of forced fold tops (Magee et al., 2019; Tian et al., 2021; Wang et al., 2022); that is, from this we can measure the total intrusion-induced displacement of the surface.

2.2. Displacement Scale

There are systematic differences in the magnitude and timeframe of displacements estimated from seismic reflection data and from contemporary geodetic observations (e.g., GNSS, InSAR, or leveling) (Figure 1c; Table S1 in Supporting Information S1) (cf. Karlstrom et al., 2018). The geometry of seismically imaged forced folds captures the total surface displacement, typically 10's–100's m, acquired over the entire or most the lifetime of shallow-level intrusions (Figure 1c) (e.g., Magee et al., 2019; Tian et al., 2021; Wang et al., 2022). Field evidence reveals igneous intrusions, from sills and dykes through to large laccoliths and plutons, can emplace and deform the host rock either in one event or through the incremental injection of discrete magma pulses (e.g., Anderson et al., 2018; Annen, 2011; Coleman et al., 2004; Glazner et al., 2004). Yet it is often difficult to determine from seismic reflection data whether displacement accrued in a single intrusion event, or incrementally through

multiple episodes of injection (e.g., Magee et al., 2017b; Reeves et al., 2018). In contrast, surface uplift at active volcanoes typically involves mm–m displacements recorded over days-to-years, reflecting only incremental recharge or growth of a magmatic system, and may be transient/reversible (at depths of ~0–15 km; Figure 1c) (e.g., Biggs & Wright, 2020; Ebmeier et al., 2018; Karlstrom et al., 2018; Menand, 2008). Larger magnitudes of uplift akin to those inferred from seismic reflection data have occasionally been observed at active volcanoes (e.g., Castro et al., 2016; Chadwick Jr et al., 2019). For example, 200 m of surface uplift across ~12 km^2 occurred over a month due to laccolith intrusion at Cordón Caulle, Chile in 2011 (Figure 1c) (Castro et al., 2016).

Our seismic reflection data do not allow us to establish whether surface displacements accrued in a single event, or incrementally due to successive emplacement of small magma pulses. We explore a snapshot of forced fold development by scaling displacement magnitudes whilst maintaining their spatial pattern; that is, this makes them similar in scale (i.e., mm–m) to surface movements often recorded at active volcanoes (Figures 1c and 1d). Such a snapshot of displacement could represent: (1) a short period of forced fold growth during one continuous intrusion event; or (2) a small-scale uplift event related to injection of a discrete magma pulse (e.g., a sill) that contributed to incremental laccolith growth and analogous to most modern deformation observations. Inherent to both end-member scenarios is the assumption that the laccolith and forced fold lateral dimensions were established early, with intrusion thickening and vertical uplift dominating after (Figure 1d). These assumptions are supported by field evidence, as well as physical and numerical modeling, showing sills often rapidly propagate laterally and inflate, which if magma supply is sufficient can cause them to develop into laccoliths (e.g., Corry, 1988; Menand, 2008; Pollard & Johnson, 1973). Even if magma supply is restricted and sills solidify, their contacts provide rheological boundaries that can capture subsequent magma pulses and grow laccoliths (or thick sills) via sequential stacking of sills with similar lateral dimensions (e.g., Annen, 2011; de Saint-Blanquat et al., 2006; Horsman et al., 2009; Menand, 2008; Morgan et al., 2008; Zieg & Marsh, 2012). Furthermore, our approach is consistent with the dimensional similarity of many ancient plutons, as well as overlap in planimetric areas of geodetically and seismically imaged displacement patterns (Figure 1c) (e.g., Cruden & McCaffrey, 2001; Karlstrom et al., 2018). These geometrical similarities suggest intrusion growth occurs via horizontal expansion before thickening (e.g., Cruden & McCaffrey, 2001; Menand, 2008).

2.3. 3D Displacement Distribution

Many elastic half-space models assume magma reservoir recharge or growth results in roof uplift and floor subsidence, as well as side-wall displacement in some solutions (e.g., Figure 1a) (e.g., Fialko et al., 2001; Mctigue, 1987; Mogi, 1958; Okada, 1985). Yet seismic reflection data, as well as field observations, reveal displacement associated with shallow-level intrusions is often preferentially accommodated by roof uplift via elastic bending (Figure 1b) (e.g., Koch et al., 1981; Magee et al., 2013; Pollard & Johnson, 1973). Where roof uplift via elastic bending is the only mechanism creating space for magma, we may expect the amplitude and volume of the forced fold relates simply to the intrusion thickness and volume, depending on its depth and pressure (Bunger & Cruden, 2011; Galland & Scheibert, 2013; Pollard & Johnson, 1973; Scheibert et al., 2017). However, if we were to invert surface displacements from uplift generated by elastic bending using elastic half-space models, our estimated source properties would assume that floor subsidence, and potentially side-wall deformation depending on model chosen, contributes to space generation (Figure 1a). In this scenario, we would expect a rectangular dislocation or penny-shaped crack analytical solution to overestimate source depth and volume change.

3. Seismic Reflection Analysis

In this section we: (a) provide the geological context of our study area; (b) describe the seismic reflection data and our decompaction method; and (c) present the decompacted surface displacement pattern of the forced fold.

3.1. Geological Setting

The Exmouth Plateau covers ~300,000 km^2 of the North Carnarvon Basin (NCB), offshore NW Australia (Figure 2a) (e.g., Direen et al., 2008; Longley et al., 2002; Stagg et al., 2004; Willcox & Exon, 1976). As Australia and Greater India separated in the Mesozoic, rifting produced normal faults that: (a) offset the Triassic, fluvio-deltaic, siliciclastic Mungaroo Formation; and (b) accommodated a thin siliciclastic sequence of Late Triassic-to-Jurassic shallow marine sandstones and siltstones (e.g., Brigadier Formation and Murat Siltstone) and the deep marine Dingo Claystone (Figure 2a–2c) (e.g., Bilal & McClay, 2022; Stagg et al., 2004; Tindale et al., 1998;

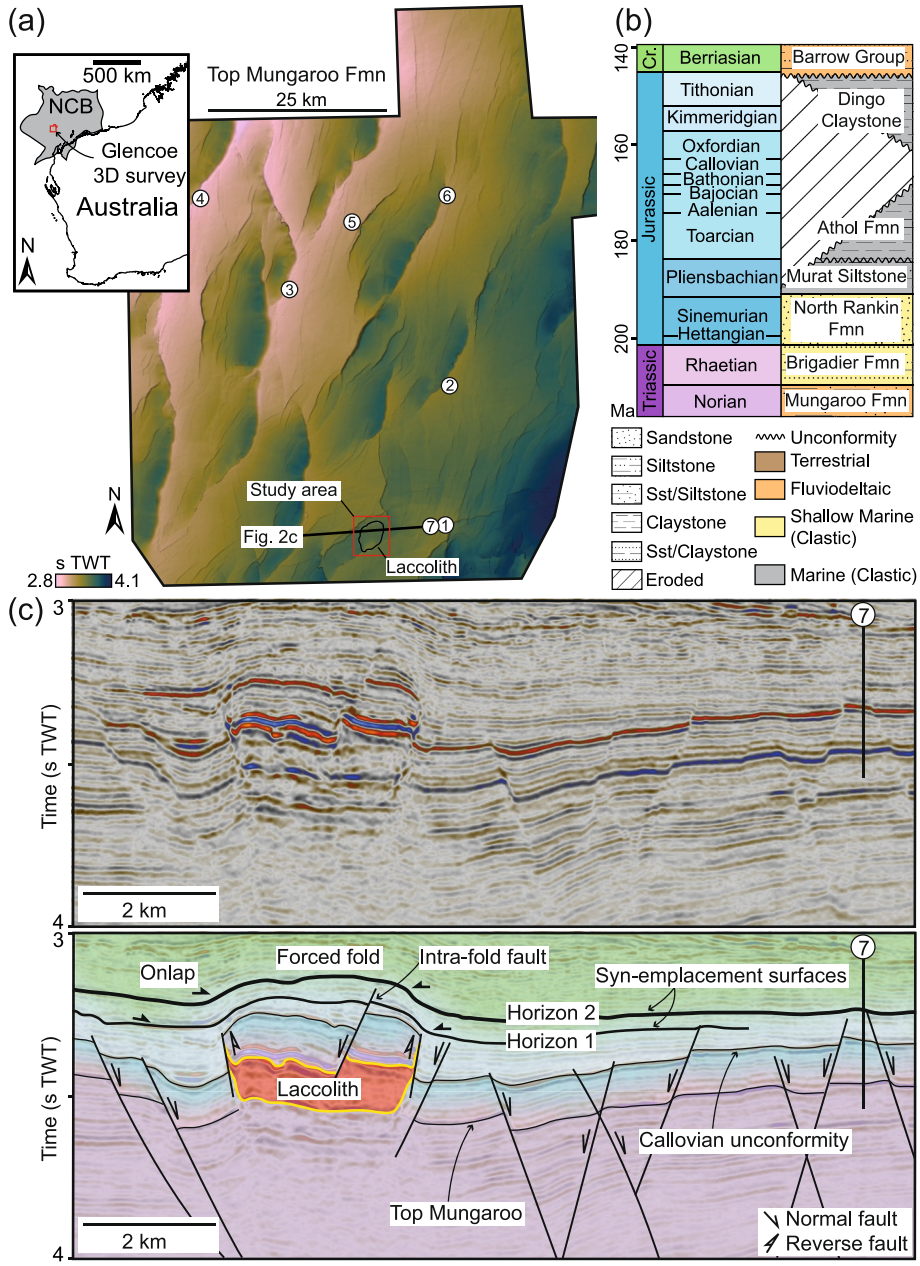

Figure 2. (a) Time-structure map of the Top Mungaroo Formation highlighting the normal fault architecture across the Glencoe 3D survey, as well as the study area and outline of the laccolith (Dobb et al., 2022). Borehole locations shown are: 1 = Chester-1ST1; 2 = Warror-1; 3 = Nimblefoot-1; 4 = Rimfire-1; 5 = Glencoe-1; 6 = Briseis-1; 7 = Chester-2. Inset: location of the Glencoe 3D survey within the North Carnarvon Basin offshore NW Australia. (b) Stratigraphic column for the study area (based on Hocking, 1992; Hocking et al., 1987; Longley et al., 2002; Tindale et al., 1998). (c) Uninterpreted and interpreted seismic reflection sections showing the structural and stratigraphic framework for the laccolith and forced fold stratigraphic framework of the studied intrusion and fold (modified from Dobb et al., 2022). See Figure 2a for location. (d) Uninterpreted and interpreted seismic reflection section, provided in color and black and white, to show evidence of probable onlap onto both horizons 1 and 2. See Figure 2a for location.

Willcox & Exon, 1976). Regional uplift and development of the Base Cretaceous unconformity toward the end of rifting preceded rapid subsidence and deposition of the Barrow Group (e.g., Paumard et al., 2018; Reeve et al., 2016; Reeve et al., 2022). Magmatism between the Kimmeridgian and Berriasian produced sills and dykes within these strata across the southern extent of the NCB (e.g., Figure 2c) (e.g., Curtis et al., 2023; Magee

et al., 2013; Magee et al., 2017b; Magee & Jackson, 2020; Norcliffe et al., 2021; Rohrman, 2013; Symonds et al., 1998).

The laccolith we study is ~4.5 × 3.0 km in plan-view and comprises a main tabular body typically ~260–320 m thick, but up to 504–617 m thick in places, and encompassing inclined sheets up to ~300 m high (Figure 2c) (Dobb et al., 2022). Seismic-stratigraphic onlap relationships onto the overlying forced fold indicate it, and the laccolith, likely formed in the Berriasian during two principal phases of activity (Figures 2c and 2d) (Curtis et al., 2023; Dobb et al., 2022); we cannot decipher whether each of these two phases of activity individually represent single events, or if they comprised multiple, incremental intrusion and deformation episodes. We also cannot discern the geometry of the intrusion developed in each phase, though we assume both were tabular, possibly reflecting stacking of discrete sills (e.g., Annen, 2011; de Saint-Blanquat et al., 2006; Horsman et al., 2009; Menand, 2008; Morgan et al., 2008; Zieg & Marsh, 2012). The first phase of laccolith and forced fold development occurred when Horizon 1 marked the contemporaneous free surface (Figures 2c and 2d). The top of the forced fold, Horizon 2, marks the second phase of laccolith emplacement and here the fold is ~5.0 × 3.5 km in plan-view, has a subtle dome-shaped morphology with a monoclinal rim, and has a current maximum amplitude (f_{max}) of ~191–268 m (Figure 2c) (Dobb et al., 2022). Development of reverse faults above the edges of the laccolith accompanied uplift at least during the first phase of laccolith emplacement, and outer-arc extensional (intra-fold) faulting occurred across both phases (Figures 2c and 2d) (Curtis et al., 2023; Dobb et al., 2022). There is no evidence for post-emplacement modification of or erosion across the forced fold (Dobb et al., 2022). Minor folding of strata occurs above Horizon 2 but this deformation is attributable to differential compaction during burial (Figure 2c) (Dobb et al., 2022).

3.2. Seismic Reflection Data

The Glencoe 3D seismic reflection survey is zero-phase and time-migrated, covering an area of ~4,042 km^2 with a line spacing of 25 m and recorded to a depth of ~8 s two-way time (TWT) (Figure 2a). Although no boreholes intersect the forced fold, we use boreholes across the Glencoe survey to (Figure 2c) (Harmer & Whelan, 2012): (a) determine the lithology of the folded strata; (b) establish a time-depth relationship for the sedimentary sequence, allowing us to depth-convert measurements from seconds TWT to meters (Figure S1 and Table S2 in Supporting Information S1); and (c) calculate the limits of separability and visibility (i.e., indicators of vertical resolution), which given a dominant frequency of 25 Hz are ~56 (±6) m and ~7 (±1) m, respectively (Dobb et al., 2022). The horizontal resolution of the time-migrated seismic reflection data is likely up to ~30 (±5) m (i.e., λ/4). We depth-convert laccolith measurements assuming the intrusion has a seismic velocity of ~5.55 (±10%) km s^{-1}, which captures the typical range of mafic igneous rocks (e.g., Magee et al., 2015; Planke et al., 2005; Skogly, 1998). Assuming the laccolith is mafic is consistent with recognition of basaltic dykes of a similar age within the local Chester-1ST1 and Rimfire-1 boreholes (Figure 2c) (Dobb et al., 2022; Magee & Jackson, 2020).

3.3. Decompaction Method

As ancient intrusions and forced folds are buried within sedimentary basins, compaction of the folded strata reduces the fold amplitude and the vertical distance between the fold and intrusion tops (i.e., emplacement depth) (e.g., Magee et al., 2019). We focus solely on the second phase of laccolith development and its corresponding displacement of Horizon 2. To remove the effects of burial-related compaction and recover the initial forced fold geometry at Horizon two (i.e., its surface displacement pattern), we decompact and backstrip the folded sequence (Magee et al., 2019). We first define a likely pre-deformation datum for Horizon 2 by removing the fold and extrapolating the regional trend of the remaining surface across this cropped area (e.g., Figure 3a). From both Horizon 2 and its pre-deformation datum, as well the top and base laccolith surfaces, we extract gridded point arrays with regular 50 m spacings. The points comprising each array have coincident x and y co-ordinates and thus just vary in their depth (z) (Figure 3a). We denote Horizon 2 depths as $z1$, with depths of its pre-deformation datum being $z2_a$; the current fold amplitude (f) at Horizon two is thus $z1 - z2_a$ (Figures 3a and 3b).

We remove the overburden, such that $z1$ becomes the new free surface ($z3 = 0$ m), and restore the current porosity (φ) of the folded sequence to its initial porosity (φ_0) using:

$$z4 - z3 = z2 - z1 - \frac{\varphi_0}{c}\left(e^{-cz1} - e^{-cz2}\right) + \frac{\varphi_0}{c}\left(e^{-cz3} - e^{-cz4}\right) \quad (1)$$

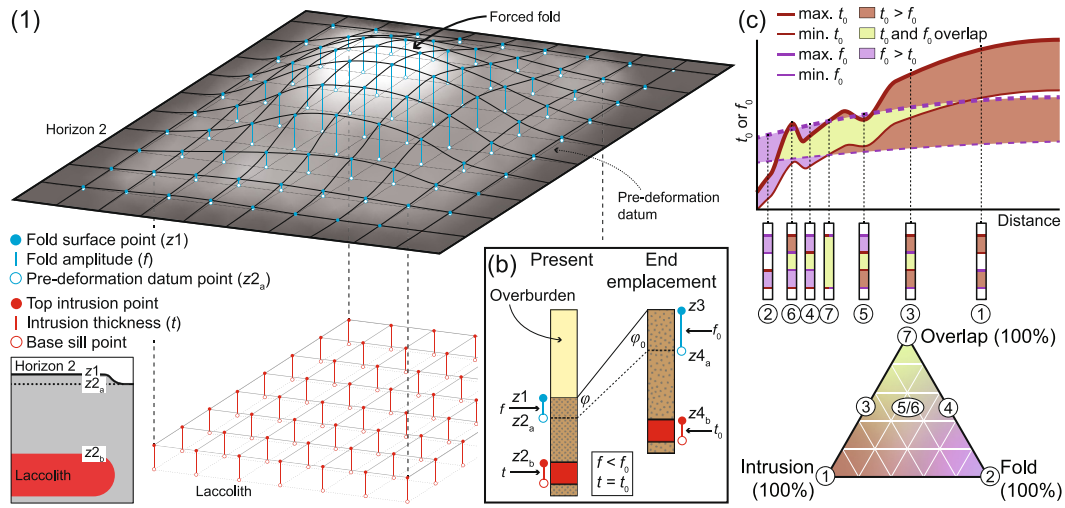

Figure 3. (a) Schematic showing how the top forced fold surface, its pre-deformation datum, and the top and base laccolith contacts are gridded into point arrays. (b) Sketch of decompaction process involving removal of the overburden and recovery of initial porosity (φ_0), such that $z1$ becomes $z3$ and the initial fold amplitude (f_0) and laccolith emplacement depth can be calculated by converting $z2_a$ and $z2_b$ to $z4_a$ and $z4_b$, respectively (based on Allen & Allen, 2013). (c) Plots showing possible relationships between the error envelopes for the initial fold amplitude (f_0) and intrusion thickness (t_0) given conservative maximum (max.) and minimum (min.) estimates for both. There are seven possible scenarios: (1) $t_0 > f_0$; (2) $t_0 < f_0$; (3) $t_0 > f_0$ but there is some overlap where we cannot know whether t_0 or f_0 is greater for that restricted parameter range; (4) $t_0 < f_0$ but there is some overlap; (5 and 6) either $t_0 > f_0$, $t_0 < f_0$, or they overlap; and (7) the error envelopes of both t_0 and f_0 completely overlap. Scenarios 1, 2, and 7 represent end-members that can be assigned to the corners of a ternary diagram, whereas scenarios 3 and 4 will lie somewhere on the intrusion-overlap or fold-overlap axis, respectively. Scenarios 5 and 6 will plot in the interior of the ternary diagram.

where c is the compaction coefficient (Figure 3b) (Allen & Allen, 2013). With Equation 1 we convert $z2$ to $z4$, such that the initial fold amplitude (f_0) of Horizon two is $z3 - z4$ (Figures 3a and 3b). Treating the laccolith top as $z2_b$ (and thus $z4_b$) also allows us to estimate laccolith emplacement depths (Magee et al., 2019). We consider that once solidified and cooled, the laccolith was incompressible, so its current thickness (t) is equivalent to its initial thickness (t_0) (Figure 3b). For simplicity, we do not account for the potential reactivation of earlier reverse faulting during the interpreted second phase of laccolith development as there is no clear evidence of this.

Our decompaction approach is limited because estimates of φ_0 and c are not available for the folded strata analyzed (Dobb et al., 2022). To account for this uncertainty, we use a range of realistic values for of φ_0 and c given that the Chester-2 borehole indicates the folded sequence comprises interbedded sandstones, siltstones, marls, and calcilutites (Harmer & Whelan, 2012). Specifically, we consider φ_0 ranges from 0.2 to 0.68, consistent with a range of siliciclastic sequences, and c ranges from 0.1 to 0.7 km (Allen & Allen, 2013; Lai et al., 2022). To compare t_0 and f_0 given our uncertainty in their input variables (e.g., seismic velocities and material properties), we calculate percentage probabilities and use a ternary plot to define where t_0 or f_0 may be greater, or if their range overlaps, at any given point (Figure 3c). As the end-members of our input parameter ranges are extreme and represent less likely scenarios, we also provide decompacted measurements considering a probable scenario where the folded succession is a muddy sandstone, consistent with local borehole data, with a φ_0 of 0.55 and c of 0.39 (Allen & Allen, 2013), and the seismic velocity of the laccolith is 5.55 km s^{-1}. All data are provided in Table S3 of Supporting Information S1.

3.4. Seismic Reflection Results

The elevation change pattern of the forced fold is broadly dome-shaped at Horizon 2 with prominent monoclinal rims (Figures 2c and 4a). Our decompaction analysis reveals that the fold here covers an area of ~17 km^2, had an initial maximum amplitude (f_{0max}) of ~189–402 m, and a volume of ~1.1–2.6 km^3 (Figures 1c and 4b). For our probable scenario, f_{0max} is ~309 m and the fold volume ~1.9 km^3 (Figure 4b). In comparison, the laccolith has an area of ~10 km^2, an initial maximum thickness (t_{0max}) of ~509–662 m, and volume of ~2.7–3.3 km^3 (Figure 4b). Regardless of uncertainty in variables used in our decompaction analysis, the laccolith seems consistently thicker

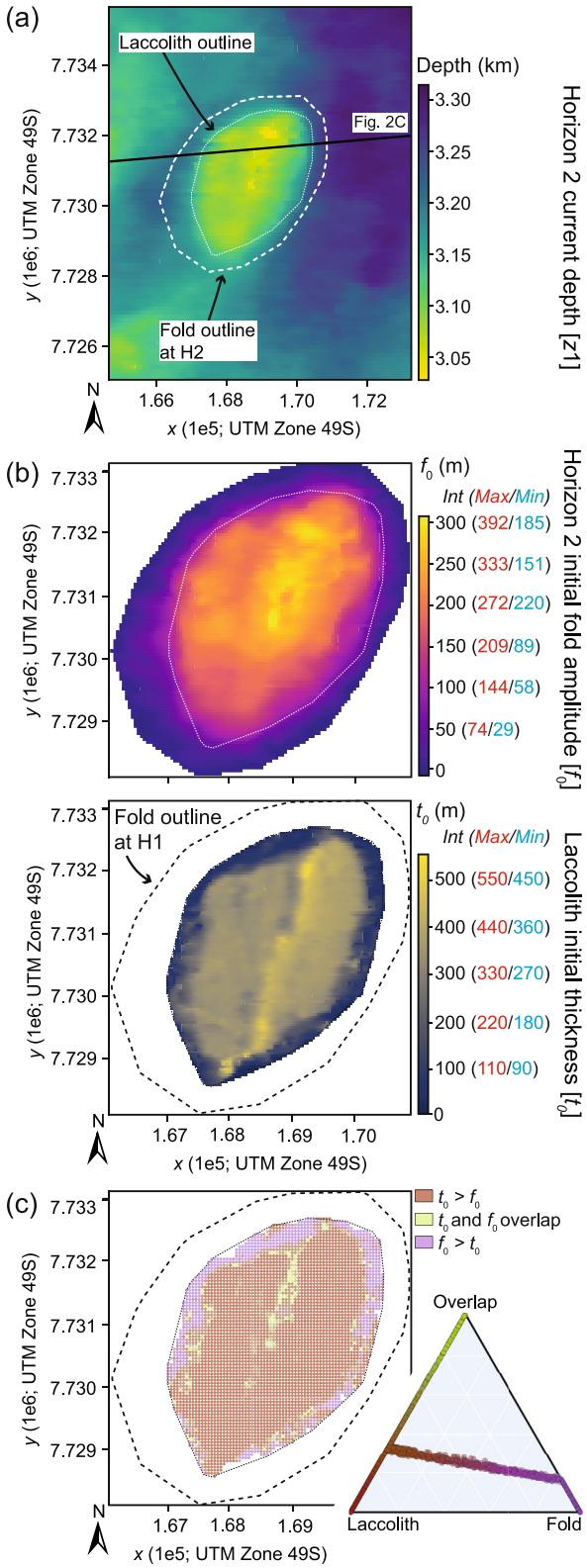

Figure 4.

than or at least broadly similar to f_0, except around its edge and partly along a NNE-trending linear zone that extends northwards from the intrusion center (Figure 4c). The mean depth of the top laccolith beneath Horizon 2 ranges from ~0.50 to 0.89 km and is ~0.76 km for the considered probable scenario; the decompacted, syn-emplacement centroid depth range of the laccolith is ~0.63–1.05 km given it is on average ~260–320 m thick (Figure 4c). For a mean laccolith length of ~3.75 km, the radius-to-depth ratio of the laccolith is thus ~3.6–6.0.

4. Analyzing Ancient Deformation

We have decompacted the surface displacement of the forced fold at Horizon 2 and quantified the underlying laccolith geometry, whilst accounting for uncertainties in our analysis. Here, we describe the modeling approach employed to constrain potential source properties from our estimated surface displacements. We recognize that some emplacement and folding occurred prior to deposition of Horizon 2 (Figure 2c), when Horizon 1 marked the contemporaneous surface (Dobb et al., 2022). The surface displacements we estimate from decompaction of Horizon 2 will therefore not wholly reflect the full geometry (volume or thickness) of the laccolith. However, we still expect estimated source location, plan-view size (e.g., radius), and emplacement depths to broadly equal those of the observed laccolith. Given the tabular geometry of the intrusion studied (e.g., Figure 2c), we test analytical solutions for bending of a thin elastic plate above shallow-level laccoliths (Galland & Scheibert, 2013) and displacements around penny-shaped crack and rectangular dislocation sources embedded within an elastic half-space (Fialko et al., 2001; Okada, 1985).

4.1. From Elevation Change to Co-Intrusive Displacements

Volcano deformation modeling aims to estimate source intrusion properties from measured surface displacements (e.g., Segall, 2010). By decompacting our seismic reflection data, we estimate the distribution of surface displacement for the forced fold (i.e., its initial geometry) and from this constrain the initial fold amplitude (f_0) (Figure 4b). These f_0 measurements describe the elevation change, that is, vertical displacement (U_Z), at any location across the forced fold (Figure 5a). To align these surface displacement estimates with data we may collect at active volcanoes, we create a triangular mesh from our Horizon two point-array and for each resolved triangle define the x and y co-ordinates of their centroid and a corresponding mean U_Z of its three vertices (Figures 3a and 5a). We can consider each of these centroids as equivalent to a leveling station; that is, instruments that solely record changes in elevation (e.g., Figure 5b) (e.g., Sigmundsson et al., 2018). By inverting this U_Z data we can thus model an end-member scenario where all

Figure 4. (a) Depth-converted structure map of Horizon 2 within the study area. (b) Initial fold amplitude and laccolith thickness maps following decompaction and backstripping of the overburden. Because we cannot know the initial porosity (φ_0) or compaction coefficient (c) of the deformed strata we calculate maximum (Max) and minimum (Min) end-members, and a probable intermediate (Int) scenario. Similarly, for the laccolith, we do not know its seismic velocity, so we calculate maximum (Max) and minimum (Min) end-members, and a probable intermediate (Int) scenario, assuming its velocity is 5.55 (±10%) km s^{-1}. (c) Map and ternary diagram depicting likely relationships between initial fold amplitude and laccolith thickness given uncertainties in input parameters.

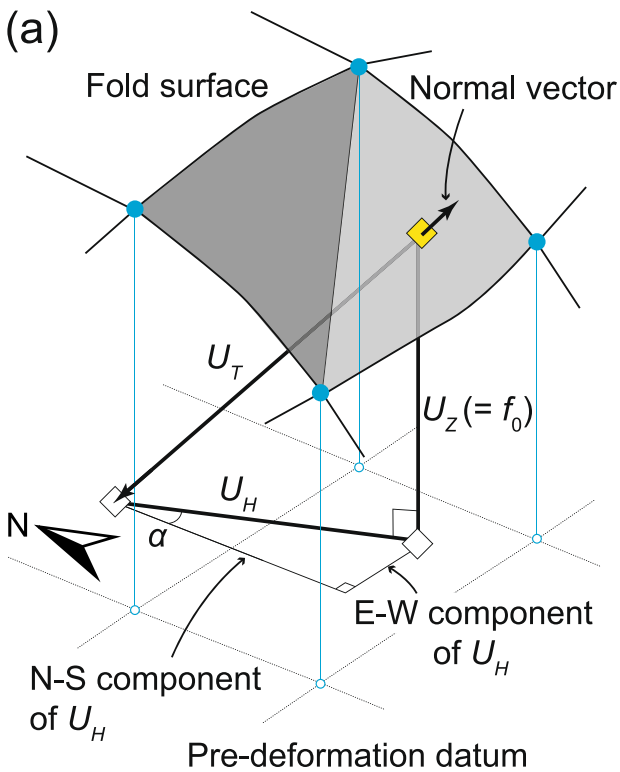

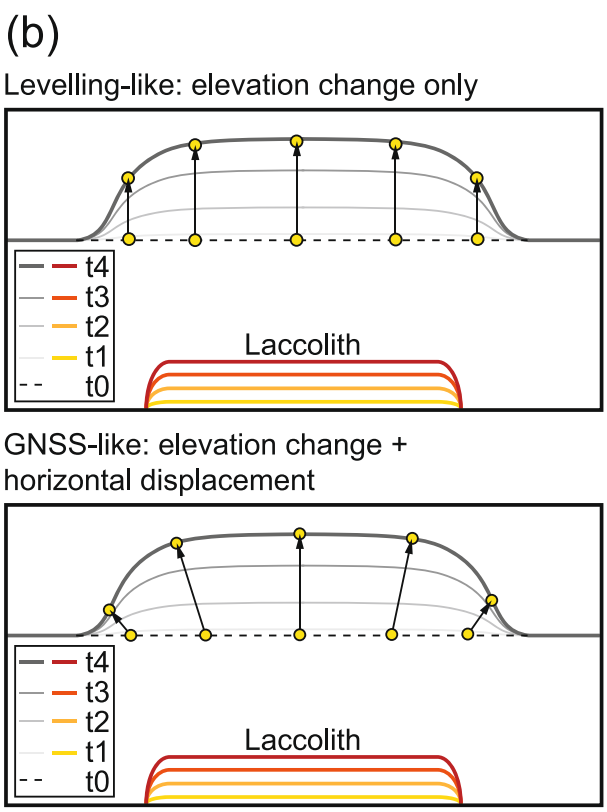

Figure 5.

displacements have a vertical trajectory (Figure 5b). Such an end-member scenario is consistent with initial sill propagation, of magma or other fluids (e.g., remobilized sand), followed by vertical inflation or sill stacking (e.g., de Saint-Blanquat et al., 2006; Morgan et al., 2008; Vétel & Cartwright, 2010).

Horizontal surface displacements (U_H) are sensitive to, and thus help constrain, source geometry (e.g., Battaglia & Hill, 2009). However, we cannot determine the occurrence or magnitude of U_H using seismic reflection data. We therefore simulate a plausible scenario by estimating horizontal displacements from our U_Z data and assuming the local pre-deformation datum followed the regional-trend topography of Horizon 2. Specifically, we project the mean normal vector of each triangle within the mesh from its centroid down to the pre-deformation datum (Figure 5a). From these vectors we can trigonometrically determine a possible U_H and its north-south and east-west components (Figure 5a). By using our estimated U_Z and U_H, we can consider each centroid as equivalent to a GNSS station; that is, instruments that record changes in elevation and lateral position (e.g., Figure 5b) (e.g., Dzurisin, 2006). Implicit to our scenario involving U_H derived from the fold surface normal is that displacement occurred along radial trajectories (Figure 5b).

Our estimated U_Z and U_H displacements represent the total surface movement associated with cumulative laccolith emplacement. However, the magnitudes of our displacements are 10's–100's m, unlike the mm–m scale deformation we observe at many active volcanoes (Figure 1d). To aid comparison between ancient and active systems, we scale our calculated displacement by 10^3, moving from m- to mm-scale deformation Figure 1d). This mm-scale scenario likely does not reflect an actual stage of forced fold growth but we treat this as a theoretical state that captures either: (a) a short period of uplift during the (near-)continuous emplacement of the laccolith; or (b) uplift associated with an injection of magma that contributed to incremental laccolith growth (e.g., Figures 1d and 5b). Our mm-scale scenario maintains the relative fold geometry, so we expect estimated source locations and emplacement depths to be broadly commensurate with measurements.

4.2. Modeling Procedure

4.2.1. Thin Plate Bending

Thin elastic plate theory describes how the flexural rigidity of a material, that is, its resistance to bending, effects the displacement of a plate as a transverse load is applied (Figure 1b) (e.g., Timoshenko & Woinowsky-Krieger, 1959). We use an axisymmetric, analytical, forward model to formulate surface displacements generated by bending of a thin elastic plate above a tabular intrusion lying on a deformable elastic foundation (Galland & Scheibert, 2013). As the observed forced fold extends beyond the laterals limits of the laccolith (Figures 2c and 4a), we expect the elastic foundation (underburden) to be softer than the overlying bending plate (Galland & Scheibert, 2013). We compare these predicted vertical and horizontal displacement profiles to those measured along a transect that extends from the center of the laccolith to the NE along its long axis. For each modeled displacement profile, we characterize its fit to our measured displacement data through R^2 and mean

Figure 5. (a) Sketch showing derivation of vertical (U_Z), horizontal (U_H), and total (U_T) displacement components for each centroid of a triangular mesh. (b) Schematic showing the difference in displacement trajectories between leveling stations, which only record vertical movements, and GNSS stations, which record the full 3D displacement field.

Table 1
Input Parameters for Thin Plate Elastic Bending Using the Analytical Solution of Galland and Scheibert (2013)

Variable description	Notation	Unit	Values	Justification
Laccolith radius	*a*	m	3,000, 4,500	Measured laccolith short and long axes
Laccolith depth	*h*	m	500, 890	Decompacted emplacement depth estimates of top laccolith
Young's modulus	*E*	*Pa*	0.01e10, 0.1e10, 1e10, 2e10	0.1–20 GPa considered reasonable for weakly lithified seafloor muddy sandstones
Pressure distribution parameter	*n*	–	0	Uniform pressure distribution
Elastic foundation stiffness	*k*	N/m3	10e5, 10e7	Poorly constrained but found reasonable by Castro et al. (2016)
Pressure at laccolith center and periphery	*P* and *Pa*	*Pa*	1e2, 1e3	Other values tried but these produced best fits. *P* and *Pa* equal to maintain uniform pressure

percentage error analyses (e.g., Castro et al., 2016). Within our models we assign Poisson's ratio (v) to equal 0.25, as is often assumed in the volcano deformation literature (see Heap et al., 2020 and references therein). Due to uncertainties in other input variables, we model a range of scenarios, constrained where possible by our data, and assume a uniform pressure distribution within the laccolith (Table 1). Other thin plate bending solutions that account for fracture propagation, magma flow, magma weight, multiple pulses, and/or plastic host rock deformation at intrusion tips are available (e.g., Bunger & Cruden, 2011; Scheibert et al., 2017; O'Hara et al., 2021; White et al., 2023). We do not utilize these solutions currently because their additional variables and associated uncertainties add further complexity while we choose to focus on first-order similarities.

4.2.2. Elastic Half-Space Modeling

For our elastic half-space analytical modeling, we primarily invert surface displacements using Geodetic Bayesian Inversion Software (GBIS) and Volcano Source Modeling (VSM) software to estimate geodetic source (intrusion) properties (Bagnardi & Hooper, 2018a; Trasatti, 2022a). We specifically use GBIS to model the proxy GNSS data as it is a more widely used software, and VSM for modeling the leveling stations as it has built-in functionality to handle these data (Bagnardi & Hooper, 2018a; Trasatti, 2022a). For computational efficiency of the elastic half-space inversions, we randomly downsample the number of modeled triangle centroids (stations) from 13,765 to 25 (Tables S4 and S5 in Supporting Information S1). To account for uncertainty in the data, we randomly assign a standard deviation error of 1–10 mm to the displacement components for each station (Tables S4 and S5 in Supporting Information S1), which is consistent with typical error magnitudes (Bagnardi & Hooper, 2018a). Within our models we assign Poisson's ratio (v) to equal 0.25, as is often assumed in the volcano deformation literature (see Heap et al., 2020 and references therein), and where relevant we arbitrarily set Young's modulus (E) to 1 GPa. In VSM we use both the Bayesian inversion (BI) and neighborhood algorithm (NA) approaches for inverse modeling (Trasatti, 2022a). For each GBIS and VSM model, regardless of the inversion method, we test 1×10^6 samples (Bagnardi & Hooper, 2018a; Trasatti, 2022a).

As a first-pass assessment of inversion validity, we present either: (1) the 2.5 and 97.5 percentiles of each intrusion variable calculated by GBIS (Bagnardi & Hooper, 2018a); or (2) the misfit calculated in VSM (Trasatti, 2022a). From the optimal source properties defined for each inverse model, we forward model the intrusion parameters to generate predicted displacements across the entire forced fold (Bagnardi & Hooper, 2018a). We then compare these predicted displacements to those of our depth-converted and decompacted fold measurements by calculating residuals (Bagnardi & Hooper, 2018a). Although our displacement data are normalized to mm-scales, we calculate the mean percentage error of these residuals at the 25 stations used in our inverse models as a relative proxy for quality of fit.

To visually compare similarities or differences in thin plate and elastic half-space analytical solution results, we also generate forward models of vertical displacement along the same NE-trending transect using penny shaped crack and rectangular dislocation solutions. Constrained by the observed laccolith location and geometry, we forward model scenarios where the source depth (h) is either 0.5 km or 0.89 km. The source radius (r) for the penny shaped crack models is either 3 km or 4.5 km, and for the rectangular dislocation models these values correspond to the source width and length, respectively. Possion's ratio (v) is assumed to be 0.25 and E is 1 GPa in

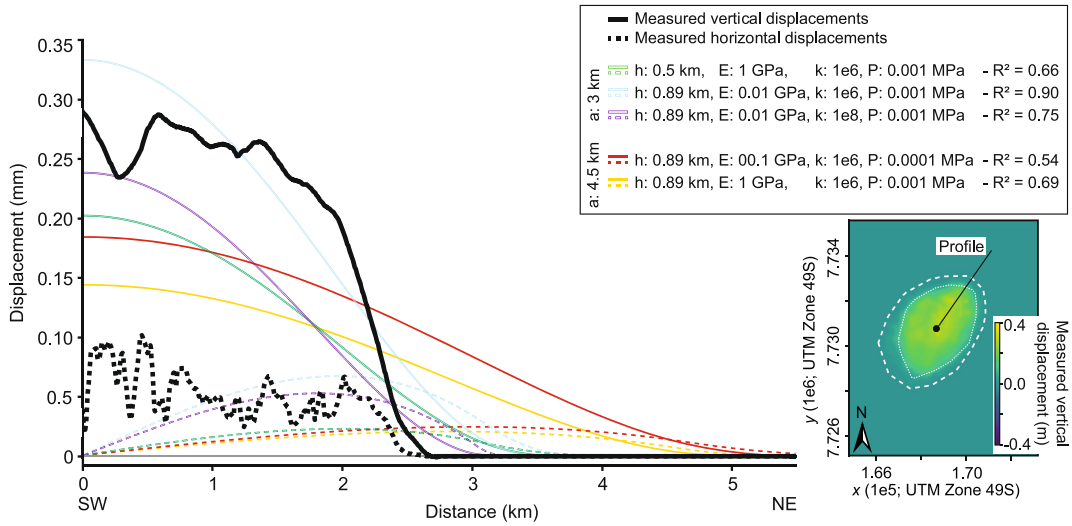

Figure 6. Plot comparing estimated vertical (U_Z) and horizontal (U_H) displacements to those modeled using a thin plate bending analytical solution (Galland & Scheibert, 2013). Only modeled input parameter combinations producing R^2 fits to the data >0.5 are plotted. The inset map highlights the plot profile extends from the fold centroid along its long axis to the NE.

all models. For the penny shaped crack and rectangular dislocation models, we iterate pressure change or source opening, respectively, to find a reasonable fits between estimated and modeled vertical displacements.

4.3. Modeling Results

4.3.1. Thin Plate Bending

Our thin plate elastic bending models all predict vertical displacements that have a bell-shaped morphology, peaking above the laccolith centroid (e.g., Figure 6; Data Set S1). Horizontal displacements reduce to 0 m above the laccolith centroid and peak toward its lateral edge (e.g., Figure 6; Data Set S1). The vertical and horizontal displacements predicted from thin-plate models all extend beyond the recognised limit of the forced fold (i.e., 2.74 km along the modeled profile) by >13%, and to greater distances for larger modeled laccoliths (e.g., Figure 6). Many input parameter combinations modeled produce extremely poor fits to measured displacements, particularly for horizontal displacements (Table 2). However, some modeled vertical displacement profiles display R^2 fits of >0.5 (up to 0.9) to measured vertical displacements, although their corresponding mean percentage errors are still >100% (Table 2). These quality-of-fit indices suggest that thin-plate bending cannot easily describe the shape of the ancient displacements (Figure 6; Table 2).

4.3.2. Elastic Half-Space Models

Most of our inverse models converge to a best-fit solution, except for models of leveling-like data (i.e., just U_Z) using the penny shaped crack solution in VSM, which does not converge for either the BI or NA methods (Table S3, Data Set S2 in Supporting Information S1). The estimated intrusion centroids for all converging penny shaped crack and rectangular dislocation models are within 500 m of the measured laccolith horizontal location (Figures 7 and 8; Table S6 in Supporting Information S1). Rectangular dislocation sources retrieved from analytical models have a similar strike and planimetric area (8.65–11.24 km^2) to the observed laccolith (~10 km^2), and there is little difference between those obtained from our simulated 3D displacements (Figures 7 and 8; Table S6 in Supporting Information S1). The rectangular dislocation sources are shorter than the laccolith as defined by the seismic reflection data, but their corners extend beyond the laccolith limits (Figures 7 and 8). Vertical displacements estimated from our seismic reflection data are greater than those modeled, except above these rectangular source corners (Figures 7 and 8); that is, the forced fold seen in the seismic reflection data has a dome-like morphology, but rectangular dislocation models would predict flat-topped deformation. Mean percentage errors for the measured and rectangular dislocation model vertical displacements are 28%–42% (Table S6 in Supporting Information S1). In contrast to the rectangular dislocation sources, the optimal penny-shaped crack source has a diameter similar to the laccolith long axis and forced fold short axis, and a planimetric area of 15.11 km^2 (Figure 8; Table S6 in

Table 2
Thin Elastic Plate Bending Results

Input variable					R2 value		Mean percentage error	
a	*h*	*E*	*k*	Overpressurea	Vertical displ.	Horizontal displ.	Vertical displ.	Horizontal displ.
(km)	(km)	(GPa)	(N/m3)		(MPa)		(%)	(%)
3.0	0.50	20.0	1.00E + 08	0.0001	−1.34	−1.14	100	104
				0.001	−1.23	−1.10	106	202
			1.00E + 06	0.0001	−1.32	−1.14	104	117
				0.001	−1.08	−1.08	159	343
		10.0	1.00E + 08	0.0001	−1.33	−1.13	100	112
				0.001	−1.13	−1.06	111	295
			1.00E + 06	0.0001	−1.30	−1.13	106	135
				0.001	−0.90	−1.02	187	534
		01.0	1.00E + 08	0.0001	−1.16	−1.07	2	250
				0.001	0.17	−0.50	179	1,747
			1.00E + 06	0.0001	−1.06	−1.05	129	379
				0.001	0.66	−0.40	466	3,073
		00.1	1.00E + 08	0.0001	0.07	−0.52	147	1,490
				0.001	–	–	1,176	14,527
			1.00E + 06	0.0001	0.36	−0.46	257	2,217
				0.001	–	–	2,506	21,875
	0.89	20.0	1.00E + 08	0.0001	−1.35	−1.14	100	99
				0.001	−1.32	−1.13	102	137
			1.00E + 06	0.0001	−1.34	−1.14	101	104
				0.001	−1.27	−1.12	122	205
		10.0	1.00E + 08	0.0001	−1.35	−1.14	100	102
				0.001	−1.30	−1.11	103	173
			1.00E + 06	0.0001	−1.34	−1.14	102	112
				0.001	−1.22	−1.09	133	288
		01.0	1.00E + 08	0.0001	−1.31	−1.12	101	151
				0.001	−0.98	−0.90	118	707
			1.00E + 06	0.0001	−1.28	−1.11	109	214
				0.001	−0.68	−0.81	222	1,364
		00.1	1.00E + 08	0.0001	−1.03	−0.92	108	580
				0.001	0.75	0.00	234	5,132
			1.00E + 06	0.0001	−0.89	−0.87	143	939
				0.001	0.90	−0.39	651	8,764
4.5	0.50	20.0	1.00E + 08	0.0001	−0.67	−0.63	116	141
				0.001	−0.29	−0.56	306	594
			1.00E + 06	0.0001	−0.64	−0.62	138	161
				0.001	−0.03	−0.54	550	807
		10.0	1.00E + 08	0.0001	−0.63	−0.62	134	187
				0.001	0.04	−0.49	502	1,078
			1.00E + 06	0.0001	−0.58	−0.61	168	221
				0.001	0.36	−0.46	885	1,434
		01.0	1.00E + 08	0.0001	−0.02	−0.49	445	1,009
				0.001	–	−0.62	4,002	9,424
			1.00E + 06	0.0001	0.15	−0.48	620	1,204

Table 2
Continued

Input variable					R2 value		Mean percentage error	
a	*h*	*E*	*k*	Overpressurea	Vertical displ.	Horizontal displ.	Vertical displ.	Horizontal displ.
(km)	(km)	(GPa)	(N/m3)		(MPa)		(%)	(%)
				0.001	–	−1.27	5,904	11,390
		00.1	1.00E + 08	0.0001	–	−0.53	3,678	9,039
				0.001	-	–	37,636	90,646
			1.00E + 06	0.0001	–	−0.82	4,628	10,121
				0.001	–	–	47,138	101,522
	0.89	20.0	1.00E + 08	0.0001	−0.71	−0.63	103	110
				0.001	−0.62	−0.61	139	263
			1.00E + 06	0.0001	−0.70	−0.63	109	119
				0.001	−0.52	−0.59	221	366
		10.0	1.00E + 08	0.0001	−0.70	−0.63	105	124
				0.001	−0.55	−0.58	176	423
			1.00E + 06	0.0001	−0.68	−0.63	116	141
				0.001	−0.39	−0.56	302	599
		01.0	1.00E + 08	0.0001	−0.57	−0.59	160	390
				0.001	0.43	−0.30	798	3,171
			1.00E + 06	0.0001	−0.50	−0.57	212	485
				0.001	0.69	−0.34	1,357	4,139
		00.1	1.00E + 08	0.0001	0.36	−0.30	712	2,982
				0.001	–	–	6,992	29,412
			1.00E + 06	0.0001	0.54	−0.30	973	3,513
				0.001	–	–	9,811	34,777

Note. Magma overpressure is calculated from input *P* and *Pa* values, and lithostatic load (see Galland & Scheibert, 2013).

Supporting Information S1). Vertical displacements modeled above the penny shaped crack source are greater than those measured above the laccolith centroid, but less than vertical displacements estimated from the seismic reflection data above the NE and SW portions of the laccolith (Figure 8). The mean percentage error for the measured and penny shaped crack model vertical displacements is 57% (Table S6 in Supporting Information S1). The estimated distribution of E-W and N-S horizontal displacement derived from our seismic reflection data is more complex than that predicted by the optimal models (Figure 8). Although there are similarities in the pattern and magnitude of measured and modeled horizontal displacements, they have mean percentage errors >140% (Figure 8; Table S6 in Supporting Information S1). Estimated centroid (emplacement) depths for the penny shaped crack and rectangular dislocation models are 0.16–0.41 km (Table S6 in Supporting Information S1), which do not overlap with the decompacted emplacement depth range of the laccolith centroid (~0.63–1.05 km).

For the forward models generated along the same transect as the thin plate bending solutions, we show that all models predict a lateral fold limit >0.5 km out from the observed fold outline (Figure 9). The rectangular dislocation profile geometries best capture the monoclinal fold limb and flat-topped fold crest geometry (Figure 9). Like the thin plate bending models, the penny shaped crack solutions produce a bell-shaped fold with limb inclinations too shallow to capture the observed fold-bounding monocline (Figure 9).

5. Discussion

5.1. Burial-Related Compaction and Intrusion-Fold Discrepancies

If space for magma emplacement is solely generated by overburden uplift, we may expect the location, shape, and size of the produced forced fold and its associated surface deformation to relate simply to that of the

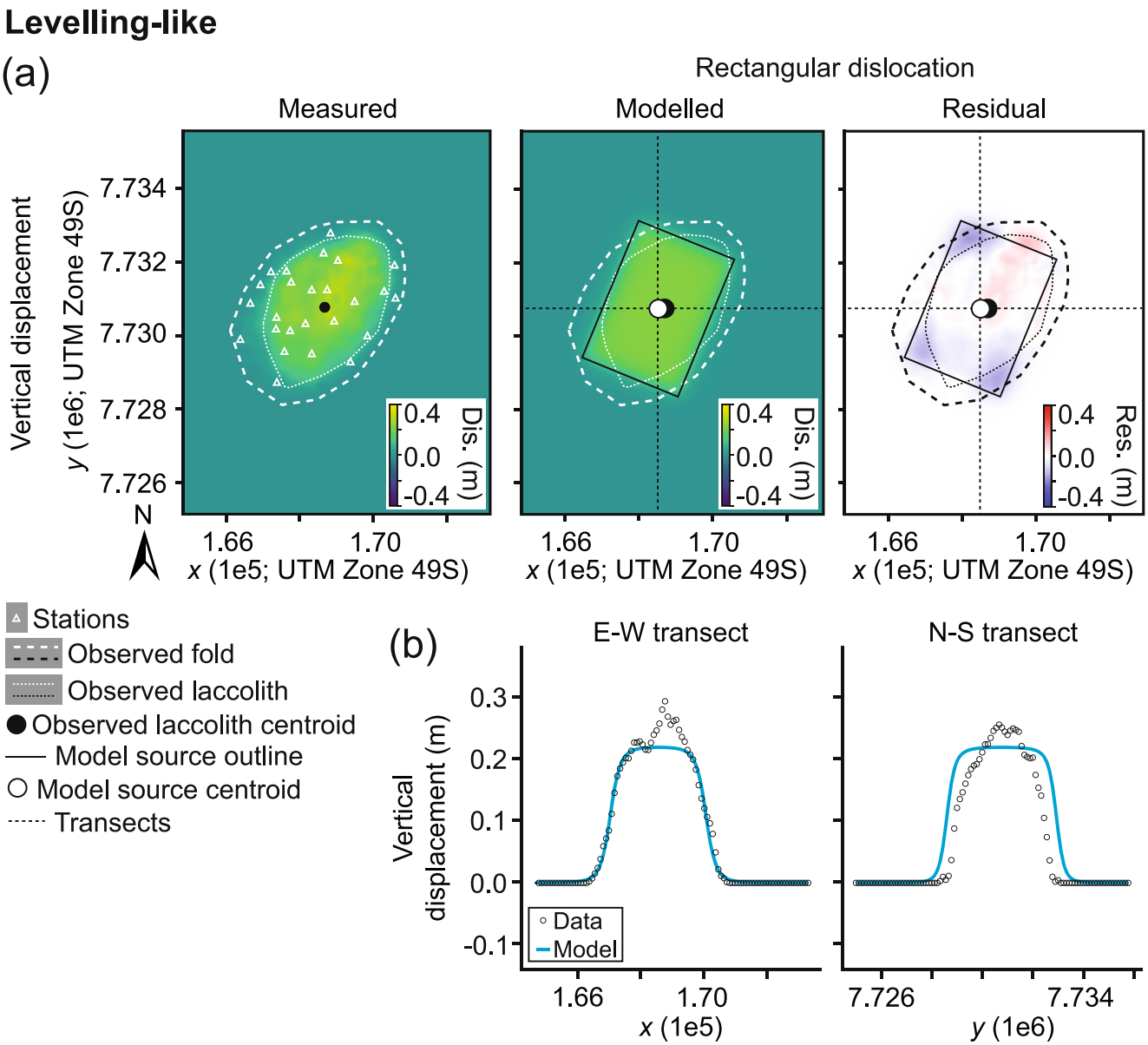

Figure 7. (a) Map of U_Z estimated from the seismic reflection data, highlighting the 25 stations selected for modeling, compared to a forward model of the optimal scenario derived from inverse modeling of leveling-like data. Residual map highlights the difference to measured displacement (displ.). (b) Transects oriented E-W and N-S through the area (see maps for locations) are also provided to compare measured and modeled displacement.

intrusion (e.g., Galland & Scheibert, 2013). The current maximum amplitude (f_{max}) of our studied forced fold at Horizon 2 is ~191–268 m (Dobb et al., 2022). Given the maximum laccolith thickness (t_{max}) is ~504–617 m, the ratio f_{max}/t_{max} is ~0.31–0.53 (Figure 10). Seismic reflection-based studies of other intrusions have recognised similar f_{max}/t_{max} relationships, some with f_{max}/t_{max} ratios as low as ~0.15 (Figure 10) (Hansen & Cartwright, 2006; Jackson et al., 2013; Magee et al., 2013, 2019). The magnitude of published f_{max}/t_{max} values, as well as field observations, have been used to suggest other space-making mechanisms contemporaneously accommodate magma emplacement in addition to uplift (e.g., Hansen & Cartwright, 2006; Jackson et al., 2013; Magee et al., 2013; Magee et al., 2019; Morgan et al., 2008; Schofield et al., 2012). These other space-making mechanisms include: (a) compressibility of shallow, especially bubbly magma (e.g., Alshembari et al., 2022); and (b) inelastic deformation of the surrounding country rock (e.g., viscoelastic, compaction) (e.g., Bonafede et al., 1986; Head et al., 2019; Morgan et al., 2008; Schofield et al., 2012). If space for magma is partly generated by one or more of these space-making mechanisms, we may expect the relationship between the

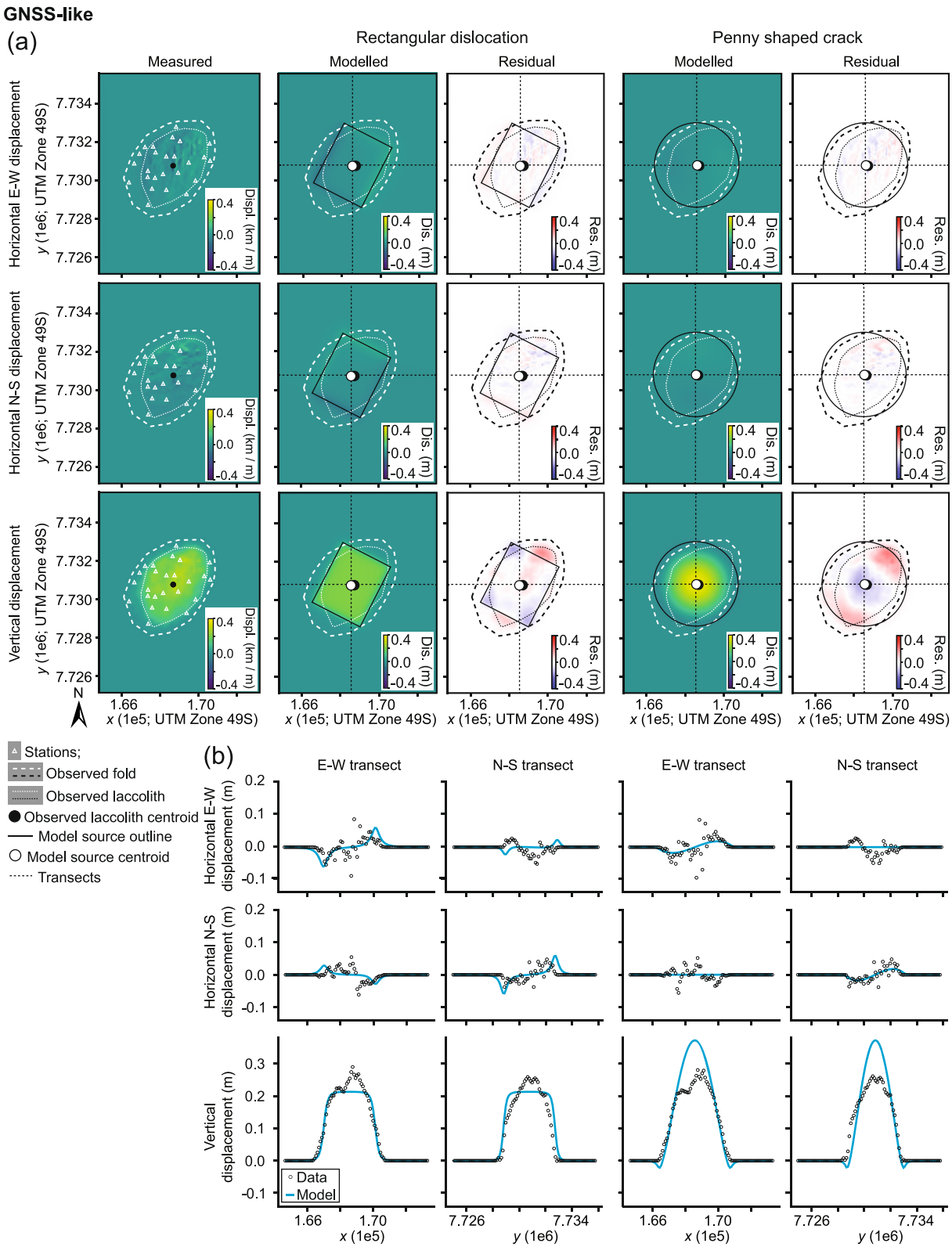

Figure 8. (a) Map of measured U_Z and estimated U_H, highlighting the 25 stations selected for modelling, compared to forward models of the optimal scenarios derived from inverse modelling of GNSS-like data. Residual map highlights the difference to measured displacement (displ.). (b) Transects oriented E-W and N-S through the area (see maps for locations) are also provided to compare measured and modeled displacement.

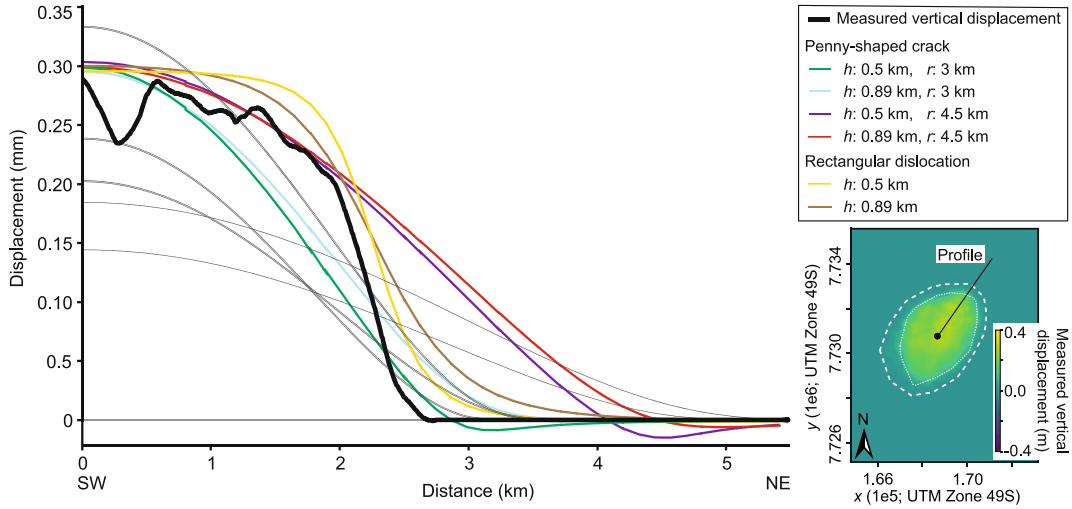

Figure 9. Plot comparing estimated vertical (U_Z) displacements to those modelled using a thin plate bending (see Figure 6), penny shaped crack, and rectangular dislocation analytical solution. The inset map highlights the plot profile extends from the fold centroid along its long axis to the NE.

location, shape, and size of any contemporaneous surface displacement and intrusion to be more complicated (e.g., Galland, 2012; Jackson et al., 2013; Magee et al., 2013). For example, source volume and/or mass may be underestimated if surface displacements do not fully reflect the space needed to accommodate intrusion growth or pressurization.

Most seismic-based analyses comparing intrusion and forced fold geometries and size are limited because they do not quantitatively account for: (1) burial-related compaction of the folded strata, which reduces fold amplitude but not the thickness of crystallized, (near-)incompressible intrusions, thereby causing $f_{max} < t_{max}$ (Magee et al., 2019); or (2) ductile strain and the upwards widening of many intrusion-induced forced folds, which to maintain their volume leads to a reduction in fold amplitude (e.g., Hansen & Cartwright, 2006; Pollard & Johnson, 1973; Withjack et al., 1990). Decompaction and backstripping techniques show estimated initial forced fold amplitudes are greater than current measurements, which in places fully accounts for $f_{max} < t_{max}$, that is, $f_0 = t_0$ (e.g., Magee et al., 2019). Here, we show that the initial maximum amplitude (f_{0max}) of the forced fold at Horizon 2 is ~189–402 m (Figures 4b and 10), so the ratio f_{0max}/t_{0max} is ~0.31–0.80, assuming $t = t_0$. Indeed, across most of the fold, except its edges, $f_0 < t_0$ (Figure 4c). With our 3D seismic reflection data, we can also calculate fold and intrusion volumes. The volume of the forced fold at Horizon 2 (~1.13–2.59 km^3) is smaller than the laccolith volume (~2.68–3.27 km^3), with the ratio between the two being ~0.35–0.97. Although errors such as changes in seismic velocity or material properties could affect our initial fold or intrusion estimates (e.g., amplitude, thickness, or volume), we adopt a conservative approach that accounts for the likely range of these uncertainties (Magee et al., 2019). We therefore have confidence that our f_0/t_0 ratio of ~0.31–0.80 and the forced fold/intrusion volume ratio of 0.35–0.97 are real. These discrepancies in forced fold and intrusion properties can, at least partly, be explained by the potential two-phase growth of the laccolith (Dobb et al., 2022). Specifically, we interpret that the forced fold at Horizon two only reflects the magma volume emplaced during the second phase of intrusion, but we compare this to the cumulative laccolith thickness and volume as we cannot separate its components. However, it is also plausible that some of the discrepancies can be attributed to: (1) the expected upwards decay of fold amplitude to maintain its volume as the fold widens (e.g., Hansen & Cartwright, 2006; Pollard & Johnson, 1973; Withjack et al., 1990); and/or (2) the occurrence of other space-making mechanisms in accommodating magma emplacement (e.g., Galland, 2012; Jackson et al., 2013; Magee et al., 2013).

5.2. Testing Volcano Deformation Models

Models represent simplifications of systems so inevitably are, to some degree, wrong (Box, 1976). We know analytical models of volcano deformation are limited by assumptions regarding intrusion geometry, material properties, and deformation behaviors (e.g., Bunger & Cruden, 2011; Fialko et al., 2001; Galland, 2012; Hautmann

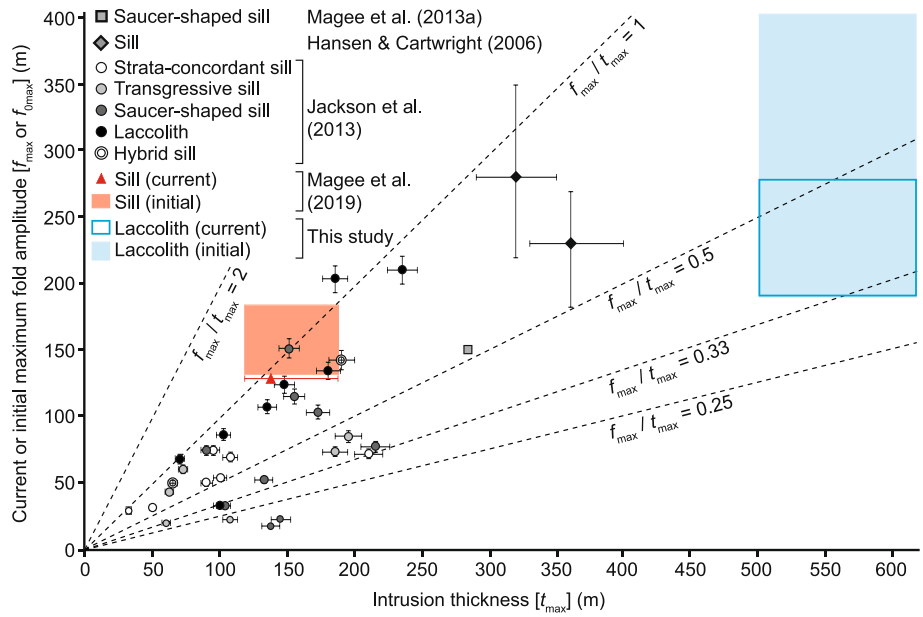

Figure 10. Plot comparing current maximum forced fold amplitudes (f_{max}) and maximum intrusion thicknesses (t_{max}) measured in seismic reflection data from the: (1) Bight Basin, offshore southern Australia (Jackson et al., 2013); (2) Exmouth Sub-basin, offshore north-western Australia (Magee et al., 2013); and (3) Rockall Basin, NE Atlantic (Hansen & Cartwright, 2006; Magee et al., 2019). Only Magee et al. (2019) decompacted and backstripped their data to also estimate initial maximum fold amplitudes; we follow this approach and given the uncertainties we consider present the possible range of the current and initial maximum fold amplitude.

et al., 2010; Hickey et al., 2013; Hickey et al., 2016; Magee et al., 2013; Masterlark, 2007; Mctigue, 1987; Mogi, 1958; Okada, 1985). Here, we compare source estimates derived from volcano deformation analytical solutions to an observed ancient intrusion imaged in seismic reflection data. Specifically, from our decompacted forced fold geometry, which represents the cumulative effects of laccolith growth, we model a plausible surface displacement scenario that represents a potential short-lived stage of fold growth (Figure 1d). Our approach maintains the fold geometry and aligns with evidence that intrusion lateral extents are established early before inflation and roof uplift dominates (e.g., Cruden & McCaffrey, 2001; Karlstrom et al., 2018). However, the fit of source estimates obtained from analytical volcano deformation models will be limited by assumptions inherent to the solutions and uncertainties within our decompaction, backstripping, and scaling method.

Despite sources of error and uncertainty, our forward and inverse models produce surface displacements and source estimates that are comparable to those measured from our seismic reflection data (Figures 6–9). For example, the vertical displacement profiles obtained from some thin plate bending forward models are broadly similar ($R^2 > 0.5$) to the observed forced fold geometry (Figure 6; Table S6 in Supporting Information S1). Inverse and forward modeling using penny shaped crack and rectangular dislocation analytical solutions also estimates source locations and planimetric geometries that broadly fit those of the observed laccolith (Figures 7–9). These similarities lend confidence to both the usage of these analytical solutions, and our scaling approach for comparing surface displacement data from active and ancient systems.

There are differences between the predicted vertical and, where applicable, horizontal displacement patterns of the analytical models relative to those acquired from the seismic reflection data (Figures 6–9). For example, if pure elastic bending accommodates uplift, we expect produced forced folds to have a bell-like geometry and a power-law relationship between its amplitude and laccolith length (Figures 1b and 11a) (e.g., Galland & Scheibert, 2013; Kerr & Pollard, 1998; Pollard & Johnson, 1973). Whilst the vertical displacement profiles obtained from our thin plate bending models are bell-shaped, as are those produced by penny shaped crack models, the observed forced fold has a prominent monoclinal rim and flatter top (Figures 2c, 6, and 9). To best-fit displacement magnitudes, we also find the spatial wavelengths of folds modeled using thin plate bending, penny shaped crack, and rectangular dislocation solutions are greater than the measured fold length (Figure 6). Finally, our results indicate that source depths (0.16–0.41 km) derived from penny shaped crack and rectangular dislocation solutions underestimate

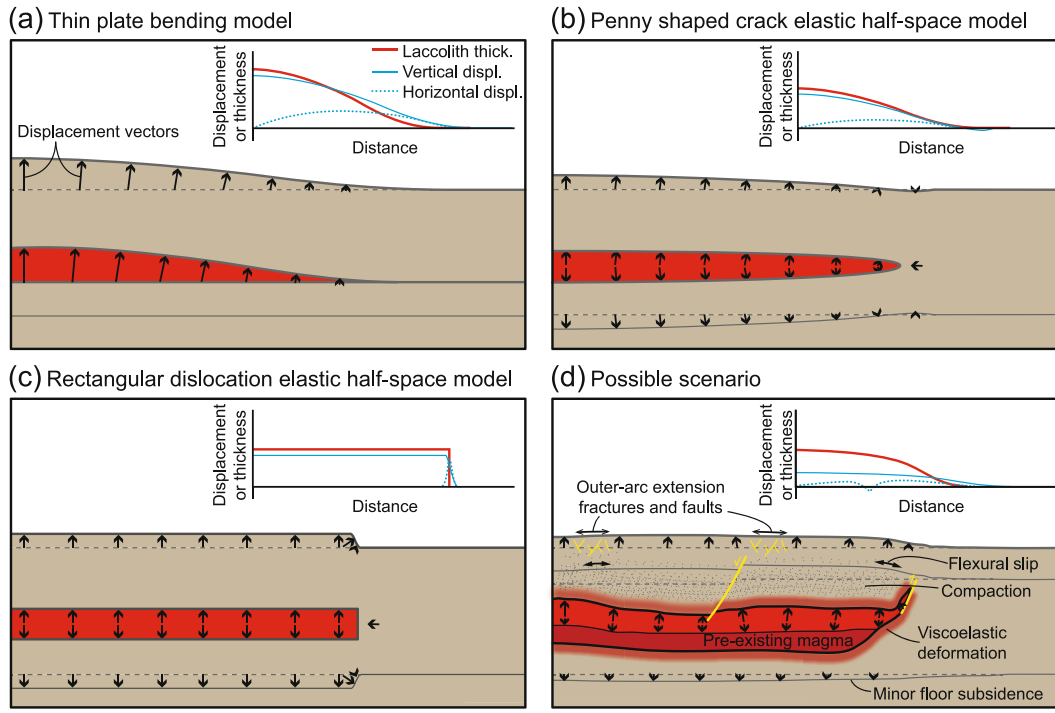

Figure 11. Schematics showing how source deformation (i.e., magma emplacement) translates into surface displacements. Inset plots describe how vertical and horizontal surface displacements (displ.) compare to the thickness (thick.) and extent of an underlying laccolith. (a) Bending of a think elastic plate above a laccolith (Galland & Scheibert, 2013). (b) Penny shaped crack elastic half-space model (Fialko et al., 2001). (c) Rectangular dislocation elastic half-space model (Okada, 1985). (d) Likely scenario where inflation of a laccolith with a complex shape is spatially accommodated by a combination of elastic deformation, of both the roof and floor, and inelastic processes such as viscoelasticity, compaction, and those related to bending (e.g., flexural slip along rock boundaries, outer-arc extension). The occurrence of elastic and inelastic deformation means surface displacements are more decoupled from the laccolith geometry (Figure 11d) than scenarios where only elastic deformation is considered (Figures 11a–11c).

measured emplacement depths (~0.63–1.05 km). Our range of emplacement depths estimated from the seismic reflection data accounts for uncertainty in our seismic interpretation and decompaction method. We thus have some confidence that this underestimate of ~0.22–0.89 km highlights a potential limitation of the penny shaped crack and rectangular dislocation models (see also O'Hara et al., 2021). In comparison, previous elastic half-space studies have found point source (Mogi) and finite volume sphere analytical solutions tend to overestimate source depths of shallow intrusions as they only work optimally when the intrusion radius-to-depth ratio is $\lesssim$0.4 or $\lesssim$0.6, respectively (Taylor et al., 2021); for context, the radius-to-depth ratio of our laccolith is ~3.6–6.0.

Variations in observed and predicted displacements probably reflect the simplicity of the analytical models, and the likelihood that displacement trajectories of surface locations were not vertical or surface-normal (cf. Figures 5b and 11). Specifically, analytical solutions cannot account for the complex geometry of natural intrusions (e.g., Galland, 2012; Poppe et al., 2024); for example, our laccolith has neither the form of a rectangular dislocation or a penny shaped crack (Figures 2c, 4b, and 11). Nor do these analytical solutions consider how the magnitude and distribution of displacement may be influenced by: (a) complex magma dynamics (e.g., magma weight, non-uniform pressure distributions) (e.g., Bunger & Cruden, 2011);: (b) host rock heterogeneity and anisotropy (e.g., layering), which changes elastic properties of rocks and for thin plate bending models reduces the elastic thickness of the overburden thereby increasing source depth estimates (e.g., Currenti et al., 2010; Geyer & Gottsmann, 2010; Hautmann et al., 2010; Manconi et al., 2007; Pollard & Johnson, 1973); or (3) contemporaneous space generation via inelastic deformation, perhaps related to extension or compression within bending layers or viscoelastic deformation adjacent to the laccolith (Figure 11d) (e.g., Jackson & Pollard, 1990; Koch et al., 1981; Morgan et al., 2008; Pollard & Johnson, 1973; Wilson et al., 2016). Overall, it is likely a combination of elastic and inelastic processes contributes to space generation for magma, complicating its translation into surface uplift (Figure 11d).

6. Conclusions

Modeling volcano deformation data is critical to eruption forecasting, hazard assessment, and understanding volcanic unrest because it allows us to estimate potential source geometries, locations, and conditions that can be used to infer magma supply characteristics. The application of analytical solutions is particularly widespread because they are computationally cheap and can be executed rapidly. Yet these models assume deformation sources have a simple geometry and the host material deforms elastically. Seismic reflection data offers a unique opportunity to test volcano deformation models as they can image ancient intrusions and overburden deformation in 3D at meter-to-decameter scales. Using seismic reflection data, we map the 3D geometry of an ancient laccolith and an overlying, dome-shaped area of uplifted strata (i.e., a forced fold) from the Exmouth Plateau, offshore NW Australia. We recover the initial, pre-burial geometry of the forced fold by decompacting and backstripping the deformed sequence using conservative estimates of material properties. Our results show that the forced fold likely had a maximum amplitude of ∼189–402 m and volume of ∼1.13–2.59 km^3 immediately after the final phase of magma emplacement. In contrast, the laccolith, which was emplaced at a depth of ∼0.63–1.05 km, has a maximum thickness of 504–617 m, and a volume of ∼2.68–3.27 km^3. The discrepancy between the fold and intrusion volumes reflects the presence of some magma prior to emplacement of the melt that instigated uplift, but also suggests other mechanisms (e.g., compaction) created space for the magma. We use thin elastic plate bending and elastic half-space, specifically penny shaped crack and rectangular dislocation, analytical solutions to forward and inverse model the recovered surface deformation of the forced fold. These models provide estimates of source (intrusion) properties that we compare to those measured directly from the seismic reflection data. To aid comparison between ancient and active magmatic systems, we scale our recovered displacement magnitudes down, whilst maintaining their spatial distribution, so they are akin to the mm–m displacements commonly observed at active volcanoes. All model estimates of laccolith size and horizontal position are reasonably similar to those measured, lending confidence to our approach. However, differences in modeled and measured surface displacements indicate the analytical solutions are limited in their ability to fit data. For example, the penny shaped crack and rectangular dislocation solutions underestimate emplacement depth by ∼0.22–0.89 km. These discrepancies in source depth likely reflect the simplicity of the models relative to the heterogeneous, anisotropic, and non-linearly elastic nature of the subsurface and the processes that accommodate emplacement (e.g., other space-making mechanisms). Overall, our work emphasizes the utility of seismic reflection data in helping assess the applicability of volcano deformation models.

Conflict of Interest

The authors declare no conflicts of interest relevant to this study.

Data Availability Statement

Contains data supplied by Natural Environment Research Council, UK. Specifically, the seismic and well data are open access and available through the National Geoscience Data Centre (Natural Environment Research Council, 2023). Table S3 in Supporting Information S1 provides the raw point data for all mapped horizons and their depth-converted versions, as well as the decompacted layer thicknesses they bound, which describe fold amplitude and emplacement depth, calculated for different parameter combinations. All modeling output files (e.g., logs of input parameters, convergence plots, optimal source estimates, etc…) for the thin plate bending and elastic half-space analytical solutions are provided in Data Seta S1 and S2. Geodetic Bayesian Inversion Software is provided by Bagnardi and Hooper (2018b) and VSM by Trasatti (2022b).

Acknowledgments
CM, SE, and JH acknowledge funding through Natural Environment Research Council (NERC) grant NE/Y000110/1. SE is also supported by NERC grant NE/R015546/1, and JH by NERC grant NE/X013944/1. We are grateful to Geoscience Australia who have made the seismic reflection and borehole data used publicly available, and to the developers of Petrel (Schlumberger), GBIS, and VSM for software provision. We thank Mark Behn for editorial handling and are very grateful to Leif Karlstrom and Joe Cartwright for their constructive and thought-provoking reviews.

References

Allen, P. A., & Allen, J. R. (2013). *Basin analysis: Principles and application to petroleum play assessment*. John Wiley & Sons.

Alshembari, R., Hickey, J., Williamson, B. J., & Cashman, K. (2022). Poroelastic mechanical behavior of Crystal mush reservoirs: Insights into the spatio-temporal evolution of volcano surface deformation. *Journal of Geophysical Research: Solid Earth*, *127*(10), e2022JB024332. https://doi.org/10.1029/2022jb024332

Anderson, P., Stevenson, C., Cooper, M., Meighan, I., Reavy, R. J., Hurley, C., et al. (2018). Refined model of incremental emplacement based on structural evidence from the granodioritic Newry igneous complex, northern Ireland. *Bulletin*, *130*(5–6), 740–756. https://doi.org/10.1130/B31756.1

Annen, C. (2011). Implications of incremental emplacement of magma bodies for magma differentiation, thermal aureole dimensions and plutonism-volcanism relationships. *Tectonophysics*, *500*(1–4), 3–10. https://doi.org/10.1016/j.tecto.2009.04.010

Bagnardi, M., & Hooper, A. (2018a). Inversion of surface deformation data for rapid estimates of source parameters and uncertainties: A bayesian approach. *Geochemistry, Geophysics, Geosystems*, *19*(7), 2194–2211. https://doi.org/10.1029/2018gc007585
Bagnardi, M., & Hooper, A. (2018b). GBIS [Software]. https://comet.nerc.ac.uk/gbis/
Battaglia, M., & Hill, D. P. (2009). Analytical modeling of gravity changes and crustal deformation at volcanoes: The long valley caldera, California, case study. *Tectonophysics*, *471*(1–2), 45–57. https://doi.org/10.1016/j.tecto.2008.09.040
Biggs, J., & Wright, T. J. (2020). How satellite InSAR has grown from opportunistic science to routine monitoring over the last decade. *Nature Communications*, *11*(1), 3863. https://doi.org/10.1038/s41467-020-17587-6
Bilal, A., & McClay, K. (2022). Tectonic and stratigraphic evolution of the central exmouth Plateau, NW shelf of Australia. *Marine and Petroleum Geology*, *136*, 105447. https://doi.org/10.1016/j.marpetgeo.2021.105447
Bonafede, M., Dragoni, M., & Quareni, F. (1986). Displacement and stress-fields produced by a center of dilation and by a pressure source in a viscoelastic half-space - Application to the study of ground deformation and seismic activity at campi-flegrei, Italy. *Geophysical Journal of the Royal Astronomical Society*, *87*(2), 455–485. https://doi.org/10.1111/j.1365-246X.1986.tb06632.x
Box, G. E. P. (1976). Science and statistics. *Journal of the American Statistical Association*, *71*(356), 791–799. https://doi.org/10.1080/01621459.1976.10480949
Bunger, A. P., & Cruden, A. R. (2011). Modeling the growth of laccoliths and large mafic sills: Role of magma body forces. *Journal of Geophysical Research*, *116*(B2), B02203. https://doi.org/10.1029/2010jb007648
Castro, J. M., Cordonnier, B., Schipper, C. I., Tuffen, H., Baumann, T. S., & Feisel, Y. (2016). Rapid laccolith intrusion driven by explosive volcanic eruption. *Nature Communications*, *7*(1), 13585. https://doi.org/10.1038/ncomms13585
Chadwick Jr, W. W., Rubin, K. H., Merle, S. G., Bobbitt, A. M., Kwasnitschka, T., & Embley, R. W. (2019). Recent eruptions between 2012 and 2018 discovered at west mata submarine volcano (NE Lau Basin, SW Pacific) and characterized by new ship, AUV, and ROV data. *Frontiers in Marine Science*, *495*. https://doi.org/10.3389/fmars.2019.00495
Coleman, D. S., Gray, W., & Glazner, A. F. (2004). Rethinking the emplacement and evolution of zoned plutons: Geochronologic evidence for incremental assembly of the Tuolumne Intrusive Suite, California. *Geology*, *32*(5), 433–436. https://doi.org/10.1130/G20220.1
Corry, C. E. (1988). Laccoliths: Mechanics of emplacement and growth. *Geological Society of America Special Paper*, *220*, 1–114. https://doi.org/10.1130/spe220-p1
Crozier, J., Karlstrom, L., Montgomery-Brown, E., Angarita, M., Cayol, V., Bato, M. G., et al. (2023). Understanding the drivers of volcano deformation through geodetic model verification and validation. *Bulletin of Volcanology*, *85*(12), 74. https://doi.org/10.1007/s00445-023-01687-4
Cruden, A. R., & McCaffrey, K. J. W. (2001). Growth of plutons by floor subsidence: Implications for rates of emplacement, intrusion spacing and melt-extraction mechanisms. *Physics and Chemistry of the Earth - Part A: Solid Earth and Geodesy*, *26*(4–5), 303–315. https://doi.org/10.1016/S1464-1895(01)00060-6
Currenti, G., Bonaccorso, A., Del Negro, C., Scandura, D., & Boschi, E. (2010). Elasto-plastic modeling of volcano ground deformation. *Earth and Planetary Science Letters*, *296*(3–4), 311–318. https://doi.org/10.1016/j.epsl.2010.05.013
Curtis, M. S., Holford, S. P., Schofield, N., & Bunch, M. A. (2023). Nature and preservation of late Jurassic breakup-related volcanism in the Carnarvon Basin, North West Shelf, Australia. *Marine and Petroleum Geology*, *153*, 106304. https://doi.org/10.1016/j.marpetgeo.2023.106304
de Saint-Blanquat, M., Habert, G., Horsman, E., Morgan, S. S., Tikoff, B., Launeau, P., & Gleizes, G. (2006). Mechanisms and duration of non-tectonically assisted magma emplacement in the upper crust: The black Mesa pluton, Henry Mountains, Utah. *Tectonophysics*, *428*(1), 1–31. https://doi.org/10.1016/j.tecto.2006.07.014
Direen, N. G., Stagg, H. M. J., Symonds, P. A., & Colwell, J. B. (2008). Architecture of volcanic rifted margins: New insights from the Exmouth-Gascoyne margin, Western Australia. *Australian Journal of Earth Sciences*, *55*(3), 341–363. https://doi.org/10.1080/08120090701769472
Dobb, E. M., Magee, C., Jackson, C. A.-L., Lathrop, B., & Köpping, J. (2022). Impact of igneous intrusion and associated ground deformation on the stratigraphic record. *Geological Society, London, Special Publications*, *525*(1), SP525-2021–2115. https://doi.org/10.1144/sp525-2021-115
Dzurisin, D. (2006). *Volcano deformation: New geodetic monitoring techniques*. Springer Science & Business Media.
Ebmeier, S., Andrews, B., Araya, M., Arnold, D., Biggs, J., Cooper, C., et al. (2018). Synthesis of global satellite observations of magmatic and volcanic deformation: Implications for volcano monitoring & the lateral extent of magmatic domains. *Journal of Applied Volcanology*, *7*(1), 2. https://doi.org/10.1186/s13617-018-0071-3
Einsele, G., Gieskes, J. M., Curray, J., Moore, D. M., Aguayo, E., Aubry, M. P., et al. (1980). Intrusion of basaltic sills into highly porous sediments, and resulting hydrothermal activity. *Nature*, *283*(5746), 441–445. https://doi.org/10.1038/283441a0
Fialko, Y., Khazan, Y., & Simons, M. (2001). Deformation due to a pressurized horizontal circular crack in an elastic half-space, with applications to volcano geodesy. *Geophysical Journal International*, *146*(1), 181–190. https://doi.org/10.1046/j.1365-246X.2001.00452.x
Galland, O. (2012). Experimental modelling of ground deformation associated with shallow magma intrusions. *Earth and Planetary Science Letters*, *317*, 145–156. https://doi.org/10.1016/j.epsl.2011.10.017
Galland, O., & Scheibert, J. (2013). Analytical model of surface uplift above axisymmetric flat-lying magma intrusions: Implications for sill emplacement and geodesy. *Journal of Volcanology and Geothermal Research*, *253*, 114–130. https://doi.org/10.1016/j.jvolgeores.2012.12.006
Garthwaite, M. C., Miller, V. L., Saunders, S., Parks, M. M., Hu, G., & Parker, A. L. (2019). A simplified approach to operational InSAR monitoring of volcano deformation in low-and middle-income countries: Case study of Rabaul Caldera, Papua New Guinea. *Frontiers in Earth Science*, *6*, 240. https://doi.org/10.3389/feart.2018.00240
Geyer, A., & Gottsmann, J. (2010). The influence of mechanical stiffness on caldera deformation and implications for the 1971-1984 Rabaul uplift (Papua New Guinea). *Tectonophysics*, *483*(3–4), 399–412. https://doi.org/10.1016/j.tecto.2009.10.029
Glazner, A. F., Bartley, J. M., Coleman, D. S., Gray, W., & Taylor, R. Z. (2004). Are plutons assembled over millions of years by amalgamation from small magma chambers? *Geological Society of America Today*, *14*(4/5), 4–12. https://doi.org/10.1130/1052-5173(2004)014<0004:apaomo>2.0.co;2
Hansen, D. M., & Cartwright, J. (2006). The three-dimensional geometry and growth of forced folds above saucer-shaped igneous sills. *Journal of Structural Geology*, *28*(8), 1520–1535. https://doi.org/10.1016/j.jsg.2006.04.004
Harmer, R., & Whelan, M. (2012). *Final well completion report, Chester-2*. National Offshore Petroleum Information Management System.
Hautmann, S., Gottsmann, J., Sparks, R. S. J., Mattioli, G. S., Sacks, I. S., & Strutt, M. H. (2010). Effect of mechanical heterogeneity in arc crust on volcano deformation with application to Soufriere Hills Volcano, Montserrat, West Indies. *Journal of Geophysical Research: Solid Earth*, *115*(B9). https://doi.org/10.1029/2009jb006909

Head, M., Hickey, J., Gottsmann, J., & Fournier, N. (2019). The influence of viscoelastic crustal rheologies on volcanic ground deformation: Insights from models of pressure and volume change. *Journal of Geophysical Research: Solid Earth*, *124*(8), 8127–8146. https://doi.org/10.1029/2019jb017832

Heap, M. J., Villeneuve, M., Albino, F., Farquharson, J. I., Brothelande, E., Amelung, F., et al. (2020). Towards more realistic values of elastic moduli for volcano modelling. *Journal of Volcanology and Geothermal Research*, *390*, 106684. https://doi.org/10.1016/j.jvolgeores.2019.106684

Hickey, J., Gottsmann, J., & de Potro, R. (2013). The large-scale surface uplift in the Altiplano-Puna region of Bolivia: A parametric study of source characteristics and crustal rheology using finite element analysis. *Geochemistry, Geophysics, Geosystems*, *14*(3), 540–555. https://doi.org/10.1002/ggge.20057

Hickey, J., Gottsmann, J., Nakamichi, H., & Iguchi, M. (2016). Thermomechanical controls on magma supply and volcanic deformation: Application to Aira caldera, Japan. *Scientific Reports*, *6*(1), 32691. https://doi.org/10.1038/srep32691

Hocking, R. (1992). *Jurassic deposition in the southern and central North West Shelf*. Geological Survey Western Australia Record, 199217.

Hocking, R. M., Moors, H. T., & Van de Graaff, W. E. (1987). Geology of the carnarvon basin, Western Australia. *State Print. Division*, *133*.

Horsman, E., Morgan, S., de Saint-Blanquat, M., Habert, G., Nugent, A., Hunter, R. A., & Tikoff, B. (2009). Emplacement and assembly of shallow intrusions from multiple magma pulses, Henry Mountains, Utah. *Earth and Environmental Science Transactions of the Royal Society of Edinburgh*, *100*(1–2), 117–132. https://doi.org/10.1017/s1755691009016089

Jackson, C. A. L., Schofield, N., & Golenkov, B. (2013). Geometry and controls on the development of igneous sill-related forced folds: A 2-D seismic reflection case study from offshore southern Australia. *Geological Society of America Bulletin*, *125*(11–12), 1874–1890. https://doi.org/10.1130/B30833.1

Jackson, M. D., & Pollard, D. D. (1990). Flexure and faulting of sedimentary host rocks during growth of igneous domes, Henry Mountains, Utah. *Journal of Structural Geology*, *12*(2), 185–206. https://doi.org/10.1016/0191-8141(90)90004-I

Karlstrom, L., Richardson, P. W., O'Hara, D., & Ebmeier, S. K. (2018). Magmatic landscape construction. *Journal of Geophysical Research-Earth Surface*, *123*(8), 1710–1730. https://doi.org/10.1029/2017jf004369

Kerr, A. D., & Pollard, D. D. (1998). Toward more realistic formulations for the analysis of laccoliths. *Journal of Structural Geology*, *20*(12), 1783–1793. https://doi.org/10.1016/S0191-8141(98)00071-6

Koch, F. G., Johnson, A. M., & Pollard, D. D. (1981). Monoclinal bending of strata over laccolithic intrusions. *Tectonophysics*, *74*(3–4), T21–T31. https://doi.org/10.1016/0040-1951(81)90189-X

Lai, L. S. H., Dorsey, R. J., Horng, C. S., Chi, W. R., Shea, K. S., & Yen, J. Y. (2022). Extremely rapid up-and-down motions of island arc crust during arc-continent collision. *Communications Earth & Environment*, *3*(1), 100. https://doi.org/10.1038/s43247-022-00429-2

Lisowski, M. (2007). Analytical volcano deformation source models. In D. Dzurisin (Ed.), *Volcano deformation: Geodetic monitoring techniques* (pp. 279–304). Springer.

Longley, I., Buessenschuett, C., Clydsdale, L., Cubitt, C., Davis, R., Johnson, M., et al. (2002). The North West Shelf of Australia–a Woodside perspective. *The sedimentary basins of Western Australia*, *3*, 27–88.

Magee, C., Bastow, I. D., de Vries, B. V., Jackson, C. A. L., Hetherington, R., Hagos, M., & Hoggett, M. (2017). Structure and dynamics of surface uplift induced by incremental sill emplacement. *Geology*, *45*(5), 431–434. https://doi.org/10.1130/G38839.1

Magee, C., Briggs, F., & Jackson, C. A. L. (2013). Lithological controls on igneous intrusion-induced ground deformation. *Journal of the Geological Society*, *170*(6), 853–856. https://doi.org/10.1144/jgs2013-029

Magee, C., Hoggett, M., Jackson, C. A. L., & Jones, S. M. (2019). Burial-Related compaction modifies intrusion-induced forced folds: Implications for reconciling roof uplift mechanisms using seismic reflection data. *Frontiers in Earth Science*, *7*(37), 37. https://doi.org/10.3389/feart.2019.00037

Magee, C., & Jackson, C. A. L. (2020). Seismic reflection data reveal the 3D structure of the newly discovered Exmouth Dyke Swarm, offshore NW Australia. *Solid Earth*, *11*(2), 579–606. https://doi.org/10.5194/se-11-579-2020

Magee, C., Jackson, C. A. L., Hardman, J. P., & Reeve, M. T. (2017). Decoding sill emplacement and forced fold growth in the Exmouth Sub-basin, offshore northwest Australia: Implications for hydrocarbon exploration. *Interpretation-a Journal of Subsurface Characterization*, *5*(3), Sk11–Sk22. https://doi.org/10.1190/Int-2016-0133.1

Magee, C., Maharaj, S. M., Wrona, T., & Jackson, C. A. L. (2015). Controls on the expression of igneous intrusions in seismic reflection data. *Geosphere*, *11*(4), 1024–1041. https://doi.org/10.1130/Ges01150.1

Magee, C., Stevenson, C. T. E., Ebmeier, S. K., Keir, D., Hammond, J. O. S., Gottsmann, J. H., et al. (2018). Magma plumbing systems: A geophysical perspective. *Journal of Petrology*, *59*(6), 1217–1251. https://doi.org/10.1093/petrology/egy064

Manconi, A., Walter, T. R., & Arnelung, F. (2007). Effects of mechanical layering on volcano deformation. *Geophysical Journal International*, *170*(2), 952–958. https://doi.org/10.1111/j.1365-246X.2007.03449.x

Masterlark, T. (2007). Magma intrusion and deformation predictions: Sensitivities to the Mogi assumptions. *Journal of Geophysical Research: Solid Earth*, *112*(B6). https://doi.org/10.1029/2006jb004860

Masterlark, T., Haney, M., Dickinson, H., Fournier, T., & Searcy, C. (2010). Rheologic and structural controls on the deformation of Okmok volcano, Alaska: FEMs, InSAR, and ambient noise tomography. *Journal of Geophysical Research: Solid Earth*, *115*(B2). https://doi.org/10.1029/2009jb006324

Mctigue, D. F. (1987). Elastic stress and deformation near a finite spherical magma body - Resolution of the point-source paradox. *Journal of Geophysical Research-Solid Earth and Planets*, *92*(B12), 12931–12940. https://doi.org/10.1029/JB092iB12p12931

Menand, T. (2008). The mechanics and dynamics of sills in layered elastic rocks and their implications for the growth of laccoliths and other igneous complexes. *Earth and Planetary Science Letters*, *267*(1–2), 93–99. https://doi.org/10.1016/j.epsl.2007.11.043

Mogi, K. (1958). Relations between the eruptions of various volcanoes and the deformations of the ground surfaces around them. *Bulletin of the Earthquake Research Institute*, *36*, 99–134.

Morgan, S., Stanik, A., Horsman, E., Tikoff, B., de Saint Blanquat, M. D., & Habert, G. (2008). Emplacement of multiple magma sheets and wall rock deformation: Trachyte Mesa intrusion, Henry Mountains, Utah. *Journal of Structural Geology*, *30*(4), 491–512. https://doi.org/10.1016/j.jsg.2008.01.005

National Environment Research Council. (2023). 3D seismic reflection surveys (Chandon and Glencoe) and borehole data from offshore NW Australia [Dataset]. *National Geoscience Data Centre*. Retrieved from https://webapps.bgs.ac.uk/services/ngdc/accessions/index.html?simpleText=glencoe#item172421

Nikkhoo, M., Walter, T. R., Lundgren, P. R., & Prats-Iraola, P. (2016). Compound dislocation models (CDMs) for volcano deformation analyses. *Geophysical Journal International*, *ggw427*.

Norcliffe, J., Magee, C., Jackson, C., Kopping, J., & Lathrop, B. (2021). Fault inversion contributes to ground deformation above inflating igneous sills. *Volcanica*, *4*(1), 1–21. https://doi.org/10.30909/vol.04.01.0121

O'Hara, D., Klema, N., & Karlstrom, L. (2021). Development of magmatic topography through repeated stochastic intrusions. *Journal of Volcanology and Geothermal Research*, *419*, 107371. https://doi.org/10.1016/j.jvolgeores.2021.107371

Okada, Y. (1985). Surface deformation due to shear and tensile faults in a half-space. *Bulletin of the Seismological Society of America*, *75*(4), 1135–1154. https://doi.org/10.1785/bssa0750041135

Parks, M., Sigmundsson, F., Drouin, V., Hjartardóttir, Á. R., Geirsson, H., Hooper, A., et al. (2023). Deformation, seismicity, and monitoring response preceding and during the 2022 Fagradalsfjall eruption, Iceland. *Bulletin of Volcanology*, *85*(10), 60. https://doi.org/10.1007/s00445-023-01671-y

Paumard, V., Bourget, J., Payenberg, T., Ainsworth, R. B., George, A. D., Lang, S., et al. (2018). Controls on shelf-margin architecture and sediment partitioning during a syn-rift to post-rift transition: Insights from the Barrow Group (Northern Carnarvon Basin, North West Shelf, Australia). *Earth-Science Reviews*, *177*, 643–677. https://doi.org/10.1016/j.earscirev.2017.11.026

Planke, S., Rasmussen, T., Rey, S. S., & Myklebust, R. (2005). Seismic characteristics and distribution of volcanic intrusions and hydrothermal vent complexes in the Vøring and Møre basins. In A. G. Doré (Ed.), *Petroleum geology: North-west Europe and global perspectives - Proceedings of the 6th petroleum geology conference* (pp. 833–844). Geological Society.

Pollard, D. D., & Johnson, A. M. (1973). Mechanics of growth of some laccolithic intrusions in the Henry Mountains, Utah, II: Bending and failure of overburden layers and sill formation. *Tectonophysics*, *18*(3), 311–354. https://doi.org/10.1016/0040-1951(73)90051-6

Poppe, S., Wauthier, C., & Fontijn, K. (2024). Inversions of surface displacements in scaled experiments of analog magma intrusion. *Geophysical Research Letters*, *51*(8), e2023GL106805. https://doi.org/10.1029/2023GL106805

Reeve, M. T., Magee, C., Jackson, C. A. L., Bell, R. E., & Bastow, I. D. (2022). Stratigraphic record of continental breakup, offshore NW Australia. *Basin Research*, *34*(3), 1220–1243. https://doi.org/10.1111/bre.12656

Reeve, M. T., Jackson, C. A. L., Bell, R. E., Magee, C., & Bastow, I. D. (2016). The stratigraphic record of prebreakup geodynamics: Evidence from the Barrow Delta, offshore Northwest Australia. *Tectonics*, *35*(8), 1935–1968. https://doi.org/10.1002/2016tc004172

Reeves, J., Magee, C., & Jackson, C. A. L. (2018). Unravelling intrusion-induced forced fold kinematics and ground deformation using 3D seismic reflection data. *Volcanica*, *1*(1), 1–17. https://doi.org/10.30909/vol.01.01.0117

Reynolds, P., Holford, S., Schofield, N., & Ross, A. (2017). The shallow depth emplacement of mafic intrusions on a magma-poor rifted margin: An example from the Bight Basin, southern Australia. *Marine and Petroleum Geology*, *88*, 605–616. https://doi.org/10.1016/j.marpetgeo.2017.09.008

Rohrman, M. (2013). Intrusive large igneous provinces below sedimentary basins: An example from the Exmouth Plateau (NW Australia). *Journal of Geophysical Research: Solid Earth*, *118*(8), 4477–4487. https://doi.org/10.1002/jgrb.50298

Scheibert, J., Galland, O., & Hafver, A. (2017). Inelastic deformation during sill and laccolith emplacement: Insights from an analytic elastoplastic model. *Journal of Geophysical Research: Solid Earth*, *122*(2), 923–945. https://doi.org/10.1002/2016jb013754

Schofield, N. J., Brown, D. J., Magee, C., & Stevenson, C. T. (2012). Sill morphology and comparison of brittle and non-brittle emplacement mechanisms. *Journal of the Geological Society*, *169*(2), 127–141. https://doi.org/10.1144/0016-76492011-078

Segall, P. (2010). *Earthquake and volcano deformation*. Princeton University Press.

Segall, P. (2013). *Volcano deformation and eruption forecasting*. Geological Society, London, Special Publications.380.

Sigmundsson, F., Parks, M., Pedersen, R., Jónsdóttir, K., Ófeigsson, B. G., Grapenthin, R., et al. (2018). Magma movements in volcanic plumbing systems and their associated ground deformation and seismic patterns. In S. Burchardt (Ed.), *Volcanic and igneous plumbing systems* (pp. 285–322). Elsevier.

Skogly, O. (1998). *Seismic characterization and emplacement of intrusives in the Vøring Basin* [MSc. Thesis]. University of Oslo.

Smallwood, J. R. (2009). Back-stripped 3D seismic data: A new tool applied to testing sill emplacement models. *Petroleum Geoscience*, *15*(3), 259–268. https://doi.org/10.1144/1354-079309-844

Sparks, R. S., Biggs, J., & Neuberg, J. W. (2012). Geophysics. Monitoring volcanoes. *Science*, *335*(6074), 1310–1311. https://doi.org/10.1126/science.1219485

Sparks, R. S. J. (2003). Forecasting volcanic eruptions. *Earth and Planetary Science Letters*, *210*(1–2), 1–15. https://doi.org/10.1016/S0012-821x(03)00124-9

Stagg, H., Alcock, M., Bernardel, G., Moore, A., Symonds, P., & Exon, N. (2004). *Geological framework of the outer Exmouth Plateau and adjacent ocean basins*. Geoscience Australia.

Stearns, D. W. (1978). Faulting and forced folding in the Rocky Mountains foreland. *Geological Society of America Memoir*, *151*, 1–38.

Symonds, P. A., Planke, S., Frey, O., & Skogseid, J. (1998). Volcanic evolution of the Western Australian Continental Margin and its implications for basin development. The Sedimentary Basins of Western Australia 2: Proc. of Petroleum Society Australia Symposium.

Taylor, N. C., Johnson, J. H., & Herd, R. A. (2021). Making the most of the Mogi model: Size matters. *Journal of Volcanology and Geothermal Research*, *419*, 107380. https://doi.org/10.1016/j.jvolgeores.2021.107380

Tian, W., Li, X. M., & Wang, L. (2021). Forced fold amplitude and sill thickness constrained by wireline and 3-D seismic data suggest an elastic magma-induced deformation in Tarim Basin, NW China. *Minerals*, *11*(3), 293. https://doi.org/10.3390/min11030293

Timoshenko, S., & Woinowsky-Krieger, S. (1959). *Theory of plates and shells* (Vol. 2). McGraw-Hill.

Tindale, K., Newell, N., Keall, J., & Smith, N. (1998). *Structural evolution and charge history of the Exmouth Sub-basin, northern Carnarvon Basin, Western Australia*. Paper presented at the The Sedimentary Basins of Western Australia 2: Proc. of Petroleum Society Australia Symposium.

Trasatti, E. (2022a). Volcanic and seismic source modeling: An open tool for geodetic data modeling. *Frontiers in Earth Science*, *10*, 917222. https://doi.org/10.3389/feart.2022.917222

Trasatti, E. (2022b). Volcanic and seismic source modeling [Software]. https://github.com/EliTras/VSM

Trude, J., Cartwright, J., Davies, R. J., & Smallwood, J. (2003). New technique for dating igneous sills. *Geology*, *31*(9), 813–816. https://doi.org/10.1130/G19559.1

van Wyk de Vries, B., Márquez, A., Herrera, R., Bruña, J. G., Llanes, P., & Delcamp, A. (2014). Craters of elevation revisited: Forced-folds, bulging and uplift of volcanoes. *Bulletin of Volcanology*, *76*(11), 1–20.

Vétel, W., & Cartwright, J. (2010). Emplacement mechanics of sandstone intrusions: Insights from the Panoche Giant Injection Complex, California. *Basin Research*, *22*(5), 783–807. https://doi.org/10.1111/j.1365-2117.2009.00439.x

Wang, C., Sun, Q. L., & Xie, X. N. (2022). Sediment deformation triggered by underlying magma intrusion. *Journal of Asian Earth Sciences*, *225*, 105045. https://doi.org/10.1016/j.jseaes.2021.105045

White, L., Malysheva, T., & Karlstrom, L. (2023). Estimation of plate parameters from vertical displacement data using a family of plate models. *The Electronic Journal of Differential Equations*, *15*.

Willcox, J., & Exon, N. J. T. A. J. (1976). The regional geology of the Exmouth Plateau. *The APPEA Journal*, *16*(1), 1–11. https://doi.org/10.1071/aj75001

Wilson, P. I. R., McCaffrey, K. J. W., Wilson, R. W., Jarvis, I., & Holdsworth, R. E. (2016). Deformation structures associated with the Trachyte Mesa intrusion, Henry Mountains, Utah: Implications for sill and laccolith emplacement mechanisms. *Journal of Structural Geology*, *87*, 30–46. https://doi.org/10.1016/j.jsg.2016.04.001

Withjack, M. O., Olson, J., & Peterson, E. (1990). Experimental models of extensional forced folds (1). *AAPG Bulletin*, *74*(7), 1038–1054.

Zieg, M. J., & Marsh, B. D. (2012). Multiple reinjections and crystal-mush compaction in the beacon sill, McMurdo dry Valleys, Antarctica. *Journal of Petrology*, *53*(12), 2567–2591. https://doi.org/10.1093/petrology/egs059